The overlooked role of westerly moisture as a source of summer rainfall in the hyperarid Atacama Desert

José Vicencio Veloso[1], Christoph Böhm[1], Jan H. Schween[1], Ulrich Löhnert[1], and Susanne Crewell[1]

[1]University of Cologne

April 16, 2024

Abstract

In the Atacama Desert, one of the driest places on Earth, the persistent absence of water preserves the record of environmental change, making it an invaluable proxy for studying the evolution of life on Earth. Due to the scarcity of in-situ measurements and difficulties in satellite remote sensing, information on precipitation characteristics is limited even for the present climate. Guided by a case study of extreme precipitation in late January 2019, we derive a conceptual framework to explain how moisture transport combined with the diurnal circulation produces rainfall. We found a synoptic pattern that we named "moist northerlies" (MNs) based on surface observations, reanalysis, and high-resolution simulation. During an MN event, moisture transport from the Tropical Pacific is observed in the lower free-troposphere in the forefront of an 850 hPa low-pressure offshore Atacama. The diurnal circulation (Rutllant Cell) transports the moist free tropospheric air inland above the coastal marine boundary layer, triggering clouds and storms. Long-term observations (1960–2020) show that most of the rainy days in the hyperarid core (75%) are triggered by MNs. A trough over the southeast Pacific and a southward displaced Bolivian High dynamically drives them, occurring more frequently during the neutral-cold phase of El Niño-Southern Oscillation (ENSO) and phases 7-8-1 of the Madden-Julian Oscillation (MJO). A trend analysis (1991–2020) reveals that summer water vapor along the subtropical west coast of South America has increased rapidly due to the MNs, enhancing summer rainfall in the Atacama. The implications of climate change and other variability modes are discussed.

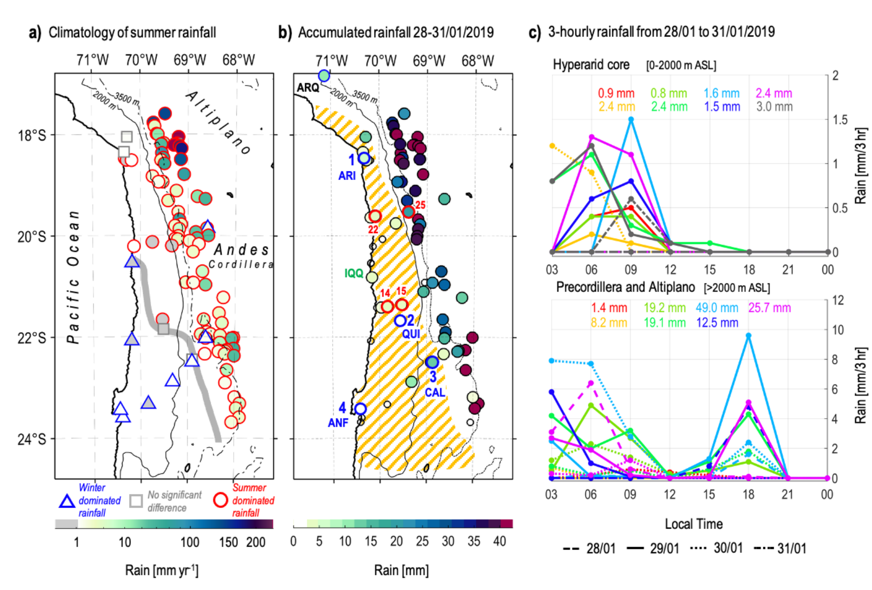

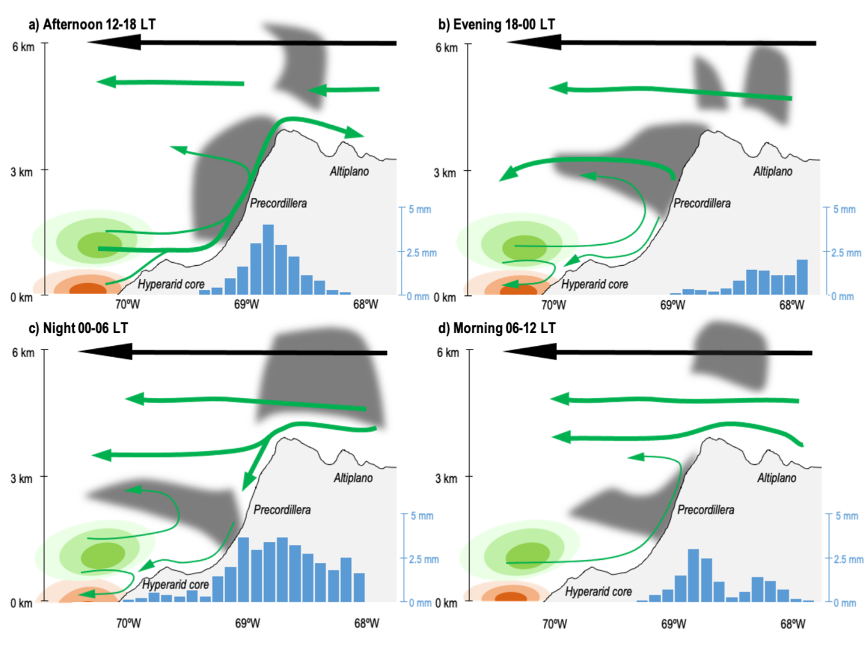
a) Afternoon 12-18 LT
b) Evening 18-00 LT
c) Night 00-06 LT
d) Morning 06-12 LT
6 km
3 km
0 km
Altiplano
Precordillera
Hyperarid core
5 mm
2.5 mm
0 mm
70ºW
69ºW
68ºW

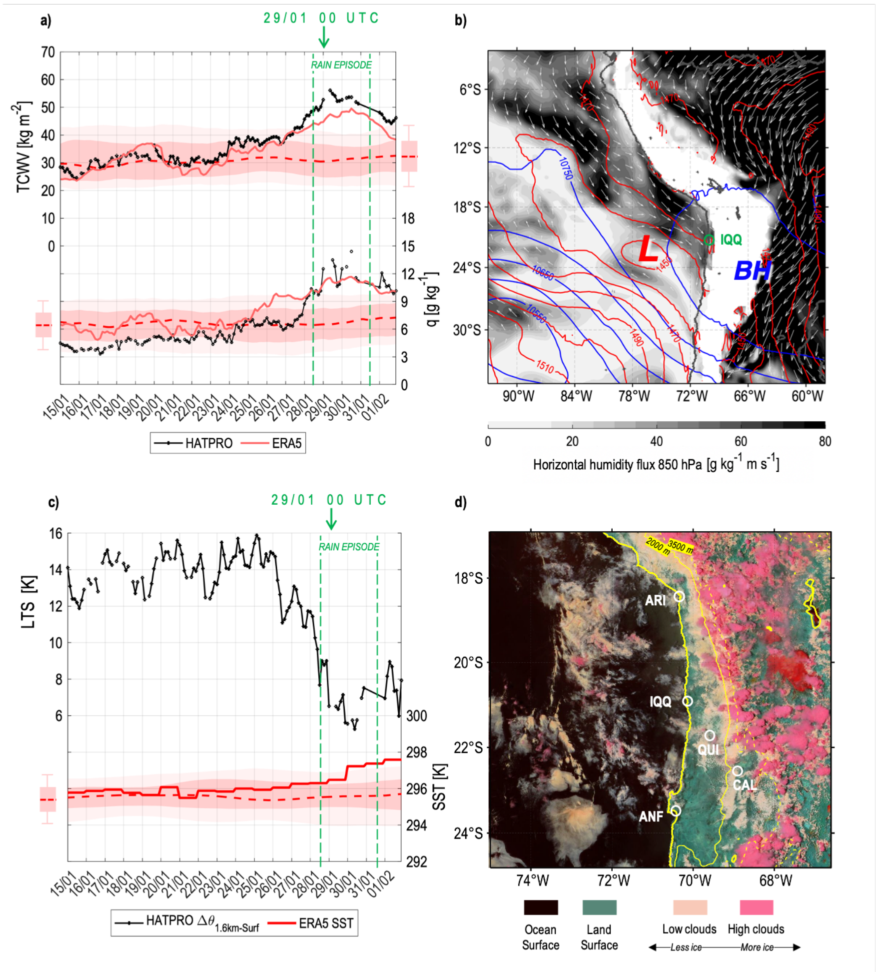
a)
29/01 00 UTC
RAIN EPISODE
TCWV [kg m-2]
q [g kg-1]
HATPRO
ERA5
b)
L
BH
IQQ
Horizontal humidity flux 850 hPa [g kg-1 m s-1]
c)
29/01 00 UTC
RAIN EPISODE
LTS [K]
SST [K]
HATPRO Δθ1.6km-Surf
ERA5 SST
d)
2000 m
3500 m
ARI
IQQ
QUI
CAL
ANF
Ocean Surface
Land Surface
Low clouds
High clouds
Less ice
More ice

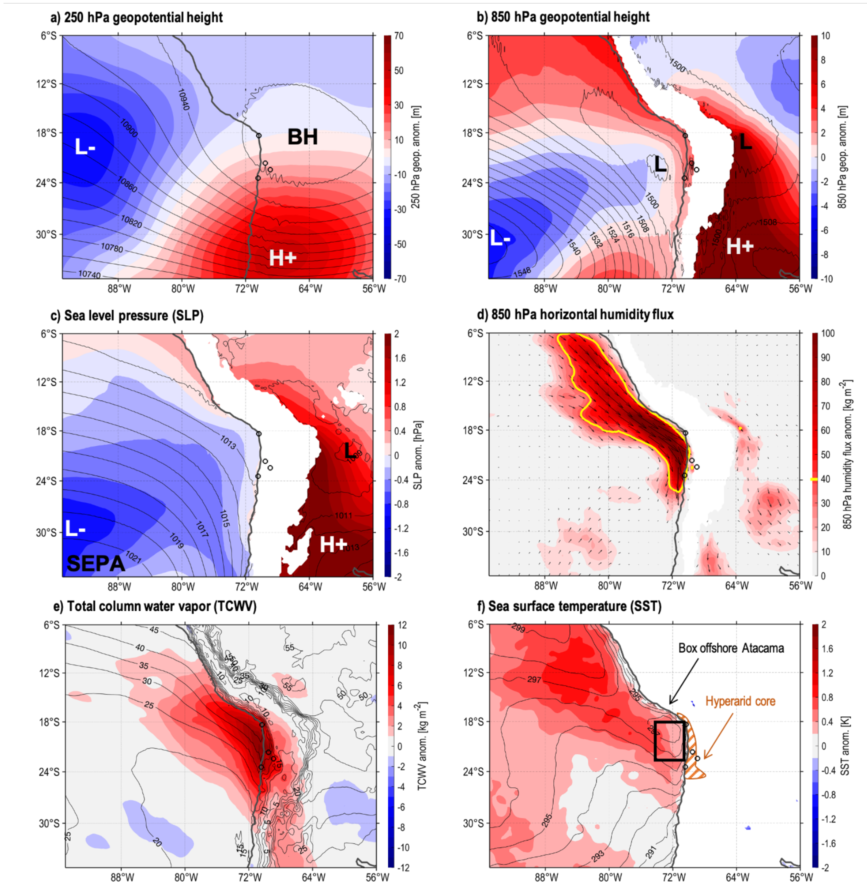
a) 250 hPa geopotential height
BH
L-
H+
250 hPa geop. anom. [m]
b) 850 hPa geopotential height
L
L-
H+
850 hPa geop. anom. [m]
c) Sea level pressure (SLP)
L
L-
H+
SEPA
SLP anom. [hPa]
d) 850 hPa horizontal humidity flux
850 hPa humidity flux anom. [kg m-2]
e) Total column water vapor (TCWV)
TCWV anom. [kg m-2]
f) Sea surface temperature (SST)
Box offshore Atacama
Hyperarid core
SST anom. [K]

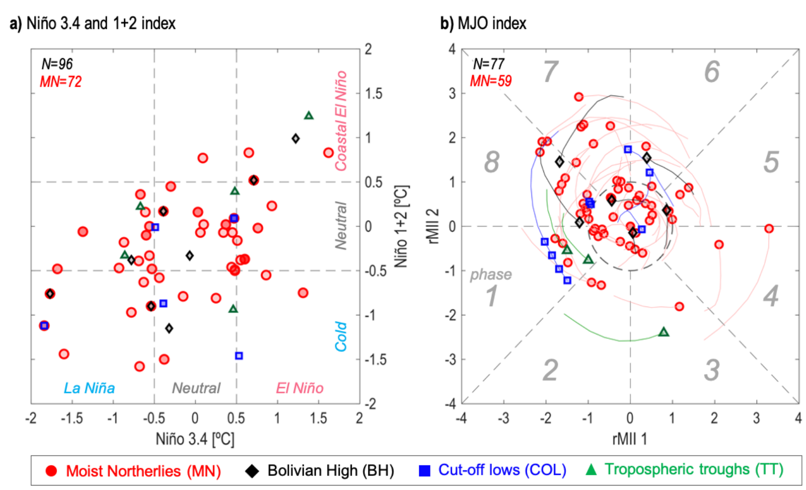
a) Niño 3.4 and 1+2 index
N=96
MN=72
Coastal El Niño
Neutral
Cold
La Niña
Neutral
El Niño
Niño 3.4 [ºC]
Niño 1+2 [ºC]
b) MJO index
N=77
MN=59
phase
rMII 1
rMII 2
Moist Northerlies (MN)
Bolivian High (BH)
Cut-off lows (COL)
Tropospheric troughs (TT)

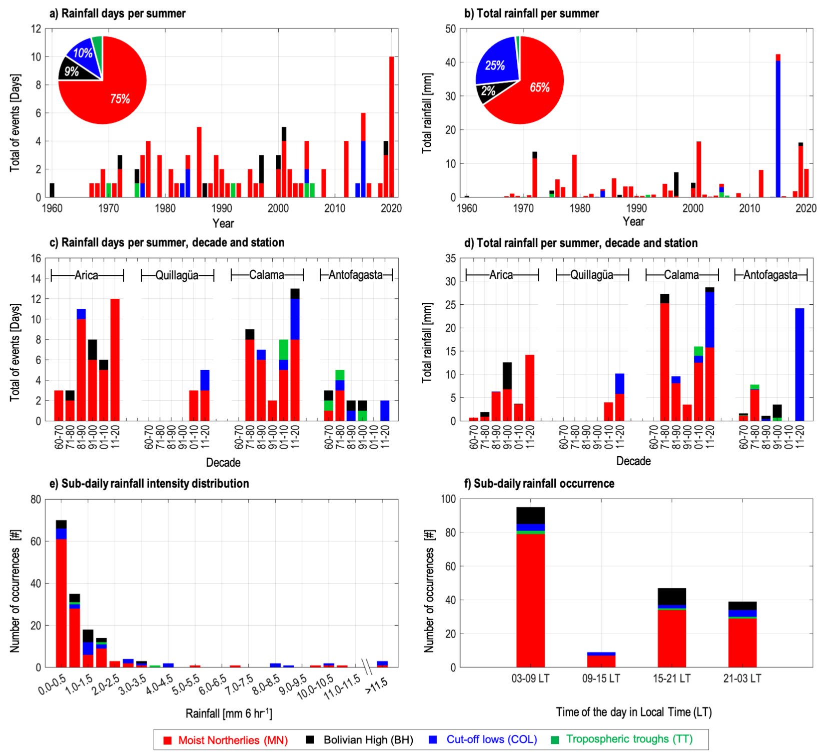
a) Rainfall days per summer
Total of events [Days]
Year
75%
9%
10%
b) Total rainfall per summer
Total rainfall [mm]
Year
65%
2%
25%
c) Rainfall days per summer, decade and station
Total of events [Days]
Arica
Quillagüa
Calama
Antofagasta
Decade
60-70
71-80
81-90
91-00
01-10
11-20
d) Total rainfall per summer, decade and station
Total rainfall [mm]
Decade
e) Sub-daily rainfall intensity distribution
Number of occurrences [#]
Rainfall [mm 6 hr-1]
0.0-0.5
1.0-1.5
2.0-2.5
3.0-3.5
4.0-4.5
5.0-5.5
6.0-6.5
7.0-7.5
8.0-8.5
9.0-9.5
10.0-10.5
11.0-11.5
>11.5
f) Sub-daily rainfall occurrence
Number of occurrences [#]
03-09 LT
09-15 LT
15-21 LT
21-03 LT
Time of the day in Local Time (LT)
Moist Northerlies (MN)
Bolivian High (BH)
Cut-off lows (COL)
Tropospheric troughs (TT)

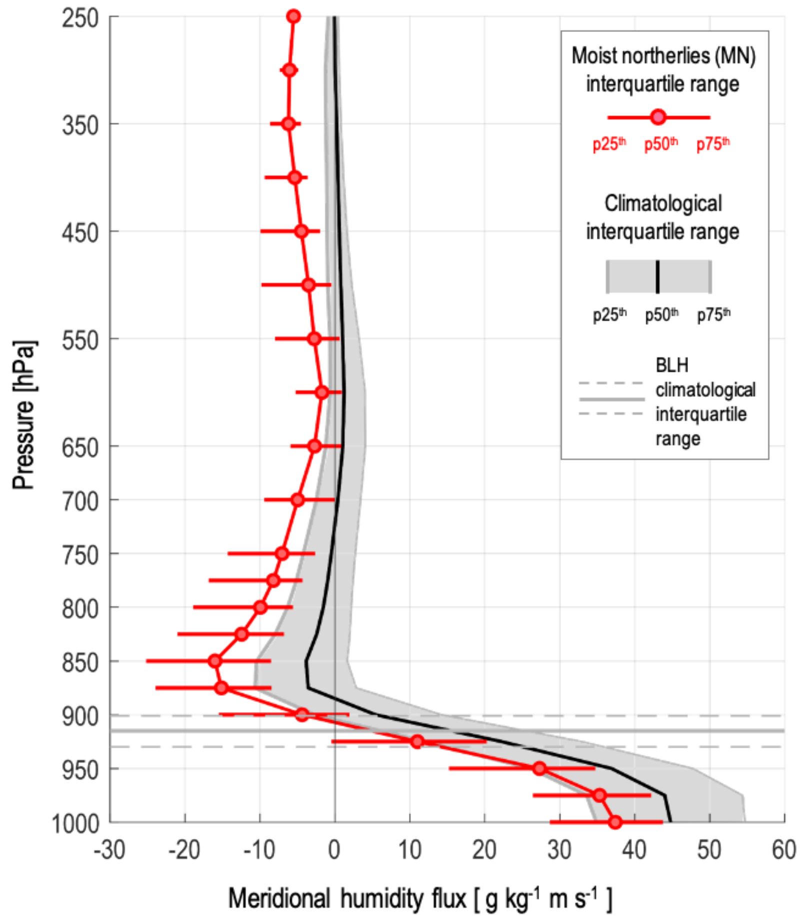
Moist northerlies (MN)
interquartile range
p25th p50th p75th
Climatological
interquartile range
p25th p50th p75th
BLH
climatological
interquartile
range
Pressure [hPa]
250
350
450
550
650
700
750
800
850
900
950
1000
-30 -20 -10 0 10 20 30 40 50 60
Meridional humidity flux [g kg-1 m s-1]

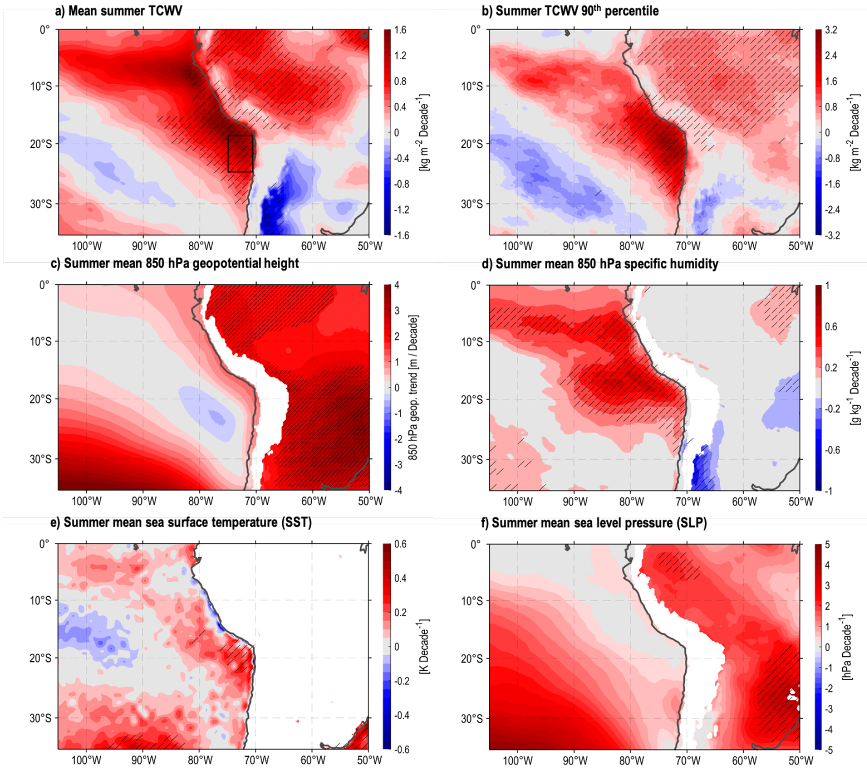

a) Mean summer TCWV
b) Summer TCWV 90th percentile
c) Summer mean 850 hPa geopotential height
d) Summer mean 850 hPa specific humidity
e) Summer mean sea surface temperature (SST)
f) Summer mean sea level pressure (SLP)
[kg m-2 Decade-1]
850 hPa geop. trend [m / Decade]
[g kg-1 Decade-1]
[K Decade-1]
[hPa Decade-1]
0°
10°S
20°S
30°S
100°W
90°W
80°W
70°W
60°W
50°W

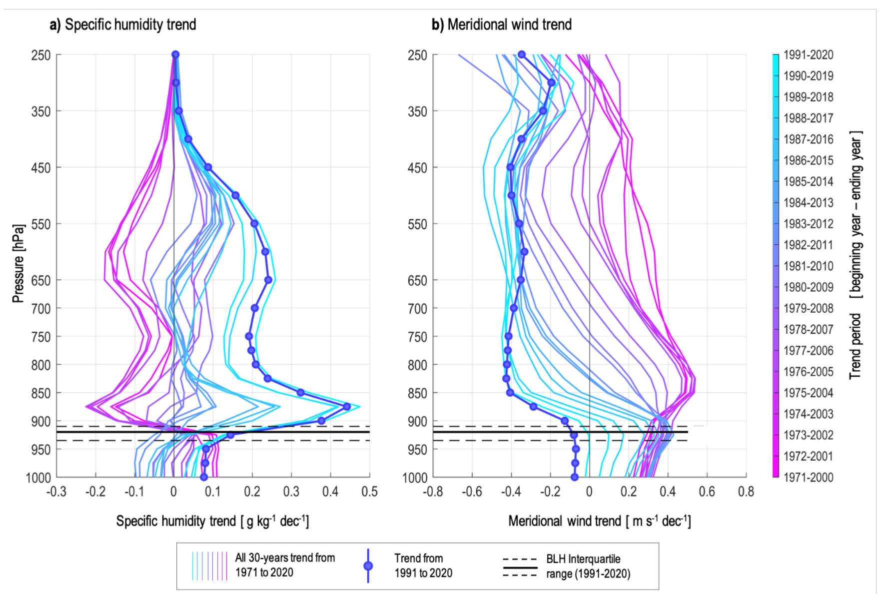

a) Specific humidity trend
b) Meridional wind trend
Pressure [hPa]
Specific humidity trend [g kg-1 dec-1]
Meridional wind trend [m s-1 dec-1]
Trend period [beginning year – ending year]
1991-2020
1990-2019
1989-2018
1988-2017
1987-2016
1986-2015
1985-2014
1984-2013
1983-2012
1982-2011
1981-2010
1980-2009
1979-2008
1978-2007
1977-2006
1976-2005
1975-2004
1974-2003
1973-2002
1972-2001
1971-2000
All 30-years trend from 1971 to 2020
Trend from 1991 to 2020
BLH Interquartile range (1991-2020)

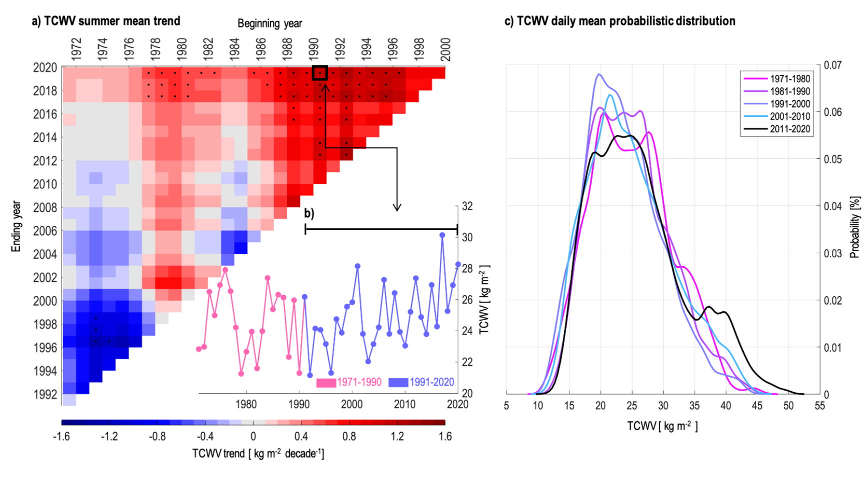
a) TCWV summer mean trend
Beginning year
Ending year
b)
TCWV [kg m-2]
1971-1990
1991-2020
TCWV trend [kg m-2 decade-1]
c) TCWV daily mean probabilistic distribution
1971-1980
1981-1990
1991-2000
2001-2010
2011-2020
Probability [%]
TCWV [kg m-2]

The overlooked role of westerly moisture as a source of summer rainfall in the hyperarid Atacama Desert

José Vicencio Veloso[1], Christoph Böhm[1], Jan H. Schween[1], Ulrich Löhnert[1], and Susanne Crewell[1]

[1]Institute of Geophysics and Meteorology (IGM), University of Cologne, Cologne, Germany

Key Points:

- Summer moisture transport, named Moist Northerlies (MNs), brings free troposphere humidity from the tropical Pacific to the Atacama
- Along with diurnal circulation, MNs lead to 75% of austral summer rainfall days in the Atacama's hyperarid core
- MN frequency has been increasing in the last decades, enhancing water vapor and rainfall in the Atacama

Corresponding author: Jose Vicencio Veloso, `jvicenc1@uni-koeln.de`

Abstract

In the Atacama Desert, one of the driest places on Earth, the persistent absence of water preserves the record of environmental change, making it an invaluable proxy for studying the evolution of life on Earth. Due to the scarcity of in-situ measurements and difficulties in satellite remote sensing, information on precipitation characteristics is limited even for the present climate. Guided by a case study of extreme precipitation in late January 2019, we derive a conceptual framework to explain how moisture transport combined with the diurnal circulation produces rainfall. We found a synoptic pattern that we named "moist northerlies" (MNs) based on surface observations, reanalysis, and high-resolution simulation. During an MN event, moisture transport from the Tropical Pacific is observed in the lower free-troposphere in the forefront of an 850 hPa low-pressure offshore Atacama. The diurnal circulation (Rutllant Cell) transports the moist free tropospheric air inland above the coastal marine boundary layer, triggering clouds and storms. Long-term observations (1960–2020) show that most of the rainy days in the hyperarid core (75%) are triggered by MNs. A trough over the southeast Pacific and a southward displaced Bolivian High dynamically drives them, occurring more frequently during the neutral-cold phase of El Niño-Southern Oscillation (ENSO) and phases 7-8-1 of the Madden-Julian Oscillation (MJO). A trend analysis (1991–2020) reveals that summer water vapor along the subtropical west coast of South America has increased rapidly due to the MNs, enhancing summer rainfall in the Atacama. The implications of climate change and other variability modes are discussed.

Plain Language Summary

The Atacama Desert, known as one of the driest places on Earth, holds vital information about how life on our planet has evolved over time because its lack of water preserves records of environmental changes. However, despite the dryness, rainfall is observed with some recurrence without being completely understood so far. This study focuses on understanding the mechanisms behind summer rain in the driest part of the Atacama Desert. We started investigating a specific extreme rainfall event in January 2019, discovering a weather pattern called "moist northerlies" (MNs) that transport moisture hundreds and thousands of kilometers from the Tropical Pacific to the desert. The moisture is transported inland during the day, triggering rain in the Atacama. Over several decades, we found that MNs cause most rainy days in the desert. These MN events seem to be influenced by larger weather patterns like the El Niño-Southern Oscillation and the Madden-Julian Oscillation. Additionally, a rapid increase in humidity has been observed along the west coast of South America in recent decades, leading to more summer rainfall in the Atacama and greening in the Andean precordillera. This study also discusses how climate change and natural variability might affect the MNs.

1 Introduction

The Atacama Desert, located on the west coast of South America (18–28°S), is well-known for its extreme hyperaridity. It is characterized by remarkably low rainfall in the hyperarid core (0.15–5 mm year^{-1}, Fig 1a, Houston & Hartley, 2003), low atmospheric moisture, and high solar radiation (Rondanelli et al., 2015). The unique desert ecosystem is a natural laboratory for studying the limits of life on Earth and the processes shaping arid environments, which are part of the main objectives of the Collaborative Research Center project 1211 "Earth-Evolution at the dry limit" (CRC1211, Dunai et al., 2020). Despite being infrequent, rainfall is observed mainly in austral winter linked with mid-latitude disturbances, e.g., cold fronts (Vuille et al., 1998) and cut-off lows (COLs, Barrett et al., 2016; Reyers & Shao, 2019). Furthermore, Moisture Conveyor Belts (MCBs) transport moisture from remote sources, such as the Amazon Basin and the tropical Pacific, across the Southeast Pacific towards the Atacama and account for 40-80% of the mean annual precipitation (Böhm et al., 2021).

The influence of the above-mentioned mechanisms decreases towards the northeast of the Atacama, resulting in a drier winter season. Consequently, the northeastern part of the desert is dominated by austral summer rainfall (Fig. 1a, e.g., Houston & Hartley, 2003; Reyers et al., 2020), for which mechanisms and moisture sources remain debated. The hyperarid core, located mainly but not exclusively <2000 m above sea level (ASL), is mostly devoid of long-term observations, making climatological investigations of precipitation challenging. Rainfall increases towards the eastern edge of the Atacama (Precordillera, 2000–3500 m above sea level, ASL) and the Andes plateau (Altiplano, >3500 m ASL), with amounts exceeding 50 mm year^{-1} almost all of which is observed in summer (Vuille et al., 1998; Garreaud, 1999). Here, the occurrence of local storms is induced by moist convection, especially when large-scale conditions strengthen easterly winds over the Andes, i.e., a southward displaced Bolivian High (BH), facilitating the transport of moisture from the interior of the continent (Garreaud & Aceituno, 2001) as part of the South American Monsoon. Some of these storms may propagate westwards from the Altiplano, causing rainfall to spill over into the desert (Reyers et al., 2020). However, the Atacama is located leeward of the episodic easterly flow, which typically leads to dry conditions by the rainshadow effect described by Houston and Hartley (2003). As a result, the spillover impact seems confined to the easternmost sector of the desert and cannot fully explain the occurrence of rainfall and storms along the hyperarid core.

Related to the easterly transport across the Altiplano, the interior continent is frequently considered to be the predominant moisture source for summer precipitation (e.g., Valdivielso et al., 2020). This is relevant because the source region determines the isotopic composition of water extracted from geological archives (Jordan et al., 2019). However, recent studies suggest the dominance of Pacific-originated moisture as the source of summer rainfall in the Atacama. For an extreme rainfall case study in the summer of 2020, Vicencio (2021) showed that strong moisture transport from the tropical Eastern Pacific at the foreside of a low-pressure system over the Southeast Pacific located in ∼850hPa led to widespread storms in the hyperarid core of the Atacama Desert. Using long-term regional climate simulations, Reyers et al. (2020) identified a cluster of rainfall events in the precordillera triggered by anomalous low-level moist air at the west of the Andes, transported upslope by the so-called Rutllant Cell (Rutllant et al., 2013). Also, Böhm et al. (2021) found a relatively high frequency of nighttime fog in the Precordillera in summer. It seems likely that westerly air-mass uplift along the steep Andes cordillera leads to saturation and cloud formation near the surface. Given the role of the Rutllant cell in transporting air from the coast to the Altiplano during the day as a result of surface heating of the Andes, it is highly conceivable that the rain and fog may originate primarily from westerly moisture rather than from an overflow of the Altiplano storms. However, to our knowledge, no study has explicitly discussed this moisture transport mechanism.

The role of large-scale oscillations in influencing summer precipitation has not been fully explored. The Madden-Julian Oscillation (MJO) has been linked to the devastating floods that occurred in central and southern Atacama in March 2015. Strong convection over the western Pacific triggered a Rossby wave pattern across the Pacific basin, forming a COL, enhancing moisture transport from the tropics, and triggering intense precipitation (Rondanelli et al., 2019). However, whether the MJO influence on precipitation is a constant pattern or an exceptional case is not clear. Similarly, the influence of the El Niño-Southern Oscillation (ENSO) on summer rainfall in the Atacama is likely limited to the Altiplano. Here, it has been shown that La Niña weakens the westerly winds in the mid-upper troposphere, increasing the easterly moisture flux and triggering precipitation over this region (Garreaud et al., 2003). The underlying moisture transport mechanisms must be investigated in more detail to study the influence of ENSO and MJO on summer rainfall in the hyperarid core.

Aside from potential large-scale patterns driving precipitation variability, underlying trends of ambient atmospheric conditions and synoptic patterns may change the rainfall regime over time. However, due to the limited availability of long-term observations, climate change's impact on summer precipitation is still unclear. Some studies based on surface weather station measurements have suggested an increase in summer rainfall in recent decades. E.g., Meseguer-Ruiz et al. (2020) found a positive trend in total accumulated rainfall for the period 1966–2015 close to Arica (∼18°S), as well in the precordillera and some areas of the Altiplano up valley from Calama (∼23°S). For a more recent period (1990–2019), Olivares (2020) confirms a generalized positive summer trend for the main stations in the hyperarid core, as well as in the precordillera and western Altiplano. Heidinger et al. (2018) discovered an increase in very intense rainfall days over Southern Peru from 1965 to 2010 by studying rainfall indices derived from satellites, indicating an increase in convective activity. These studies emphasize the importance of investigating long-term changes in moisture supply in the hyperarid core of Atacama and its potential impacts on precipitation.

We hypothesize that austral summer rainfall events in the hyperarid core of the Atacama are mainly triggered by moisture from the Pacific Ocean. To test this hypothesis, we first analyze an extreme precipitation event that occurred in late January 2019. We apply reanalysis data aided by regional-scale high-resolution weather simulations, ground-based remote sensing, and weather stations to mitigate the effects of the complex topography of the Atacama and Andes Cordillera. Second, we perform a climatological analysis (1960-2020) by identifying rainfall days in the hyperarid core from representative weather stations. We classify the circulation patterns for each day by their similarities. We conclude our research by investigating trends in moisture and circulation patterns along the Southeast Pacific that could explain the observed changes in summer rainfall.

2 Data and methods

2.1 Rain gauges and remote sensing

For the 2019 case study, we use daily accumulated rainfall for the period from 28 to 31 January 2019 for 84 stations in the Atacama (17-24°S) provided by the Center for Climate and Resilience Research (CR2: http://explorador.cr2.cl). These stations are located in the hyperarid core of Atacama (<2000 m ASL), the Precordillera (2000-3500 m ASL), and Altiplano (>3500 m ASL, Fig. 1b). To gain insight into Atacama's surface circulation, we use specific humidity, wind, and rainfall from a group of four weather stations available via the Collaborative Research Centre database (CRC1211, Hoffmeister, 2018). All variables are provided as 10-minute averages, and hourly averages are calculated for our analysis. The weather stations shown in Fig. 1b are labeled as 14 (Salar de Llamara), 15 (Quebrada de Mani), 22 (Cerro San Antonio), and 25 (Quebrada de Soga).

From a one-year field campaign at Iquique Airport (IQQ, 20.54°S, 70.18°W, Fig. 1b) total column water vapor (TCWV) and low-resolution vertically resolved specific humidity and potential temperature are used for the January 2019 case study. These data are retrieved from measurements by a microwave radiometer (MWR), specifically a 14-channel Humidity and Temperature Profiler (HATPRO, Rose et al., 2005). It performed high-frequency measurements (1 s) of brightness temperatures in the microwave range, from which TCWV and humidity profiles are derived (more details in Schween et al., 2022). We also derived the Low Troposphere Stability (LTS) as the difference between the potential temperature at 1.5 km ASL and the surface temperature, measured by HATPRO.

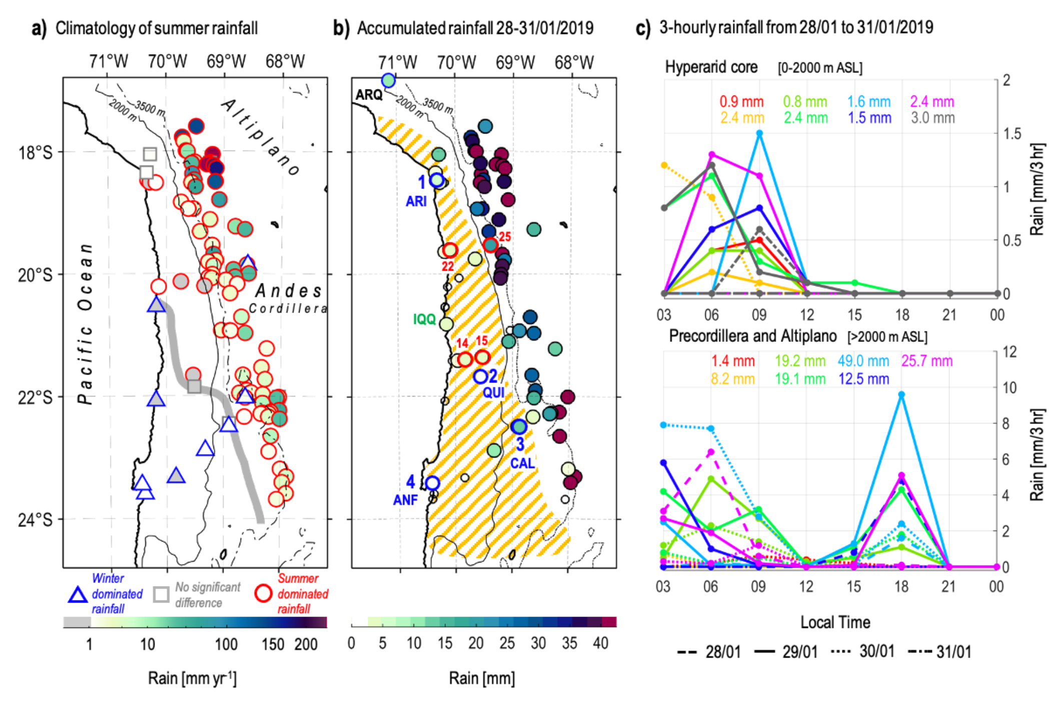

Figure 1. (a) Geographical location of the Atacama Desert and observed mean summer (December-March) rainfall from 1991-2020 for 111 rain-gauges (color-filled circles, in mm yr^{-1}). The gray solid line indicated the approximate border between winter (April-November) dominated rainfall to the south (blue triangles) and summer (December-March) dominated rainfall to the north (red circles). If the difference is not significant (less than 10%), the station is shown as a gray square. (b) Accumulated rainfall from 28–31 January 2019 for 85 rain gauges (color-filled circles, in mm). Red circles denote the four CRC1211 weather stations used for the 2019 case study (stations 14, 15, 22, and 25). Blue circles show the location of the four long-term weather stations: Arica (1 ARI), Quillagua (2 QUI), Calama (3 CAL), and Antofagasta (4 ANF). The location of Arequipa (ARQ) is presented in a black circle. In panels (a) and (b), black lines represent the coastline and terrain altitude at 2000 and 3500 m ASL. The hyperarid core is shown in (b) with a yellow hatch for areas with an annual mean less than 5 mm yr^{-1}. (c) 3-hourly accumulated rainfall between 28 and 31 January 2019 (colored lines) for 15 weather stations in panel (b) with hourly accumulated rainfall available, divided in the hyperarid core (upper panel) and Precordillera and Altiplano (bottom panel) for each day between 28–31 January 2019. The total accumulated rainfall is given in colored numbers at the top panel.

For the climatological analysis, we use daily accumulated rainfall from four weather stations with continuous records from 1960–2020 to identify rainy days in the Atacama's hyperarid core and Precordillera. The stations are Arica (1 ARI, 50 m ASL), Quillagua (2 QUI, 809 m ASL), Calama (3 CAL, 2321 m ASL), and Antofagasta (4 ANF, 112 m ASL), shown in Fig. 1b. Data were obtained from the Direccion Meteorologica de Chile (DMC) for stations 1, 3 and 4, for which 6-hourly precipitation is also available but restricted to the period 1964–2020. From the Direccion General de Aguas (DGA), we obtained daily rainfall for station 2. Using the set of four weather stations, we identified summer (December–March) rainfall days in the Atacama when more than 0 mm is recorded at least for one station per day. For example, if 2 stations recorded rainfall on the same day, it is considered as 1 rainfall day. In the 60 years, 96 summer rainfall days were detected (∼1.6 events per summer), and they are listed in Table S1.

2.2 Regional climate model and reanalysis

We apply data from the ERA5 reanalysis (Hersbach et al., 2020) of the European Centre for Medium-Range Weather Forecasts (ECMWF). The reanalysis has a time resolution of 1 hr and horizontal resolution of 0.25x0.25° latitude-by-longitude. We use the data from 1960 to 2020, only for the summer period (December–March). The surface-level variables are listed as follows: TCWV, sea surface temperature (SST), boundary layer height (BLH), and sea level pressure (SLP). The pressure level variables (1000–250 hPa) correspond to vertically resolved specific humidity, temperature, horizontal wind, and geopotential height. We derive the horizontal humidity flux as the specific humidity times the horizontal wind for each pressure level.

Considering the rainy days in the Atacama detected from weather stations from 1960–2020, we use ERA5 to composite daily means for each rainy day of the synoptic conditions for TCWV, 850 and 500 hPa geopotential height and humidity flux, and 500 hPa geopotential height and winds. We then perform a subjective classification, grouping the rainfall cases according to similar synoptic features in the lower and upper free troposphere. An example of one case of rainfall and its classification according to the synoptic pattern is shown in Figure S1. The characteristics of the 96 identified rainfall days are available in Supporting Information 1.

To complement point observations and the coarse ERA5 resolution, we use the Weather Research and Forecasting Model (WRF, Skamarock et al., 2008) for a simulation of the Atacama desert. Via a double one-way nesting, a horizontal resolution of 6 km is achieved for the output in the inner domain (17-27°S, 74-67°W) and a temporal resolution of 3 hr. This simulation is an update from a previous long-term WRF simulation performed by Reyers (2018) driven by ERA-Interim and 10 km resolution. The 6-km WRF simulation performs well for precipitation in the hyperarid core (e.g., Wennrich et al., 2024), and provides a more realistic representation of meteorological conditions over the Atacama due to a much better resolution of the complex topography (i.e., Andes Cordillera) than ERA5. From this simulation, we use specific humidity, horizontal and vertical winds, specific cloud liquid water content, and precipitation for the January 2019 case study.

2.3 Large-scale oscillations

To investigate the potential impact of ENSO on summer rainfall within the hyperarid core, we obtain monthly SST anomalies for the Niño 3.4 and Niño 1+2 regions. Both indices are based on the Extended Reconstructed Sea Surface Temperature version 5 (ERSSTv5, Huang et al., 2017), available from 1950 to nowadays, and obtained from the NOAA's Climate Prediction Center database (`https://www.cpc.ncep.noaa.gov/data/indices/`). Due to the SST warming in the Pacific Basin (L'Heureux et al., 2013), the Niño 3.4 index has been detrended by NOAA using centered 30-year base periods, moving every five years. The Niño 3.4 and 1+2 index correspond to the average SST anomalies of the Central Pacific (5°N-5°S, 170-120°W) and the Eastern Tropical Pacific (0-10°S, 90-80°W).

For the MJO, we use the real-time Multivariate Index for tropical Intraseasonal oscillations (rMII, Wang et al., 2022). This index defines the intensity of the MJO as the leading Empirical Orthogonal Functions (EOF, rMII 1 and rMII 2) of the projection of 9-day running average anomalies of the eastward filtered Outgoing Longwave Radiation (OLR), and zonal winds at 850 hPa and 200 hPa. The index is available from 1979 to nowadays and is obtained from the NOAA Physical Science Laboratory (`https://www.psl.noaa.gov/mjo/mjoindex/`). The location of the anomalous convective area that circles the Planet eastward (Madden & Julian, 1972) is classified into phases labeled from

1 to 8, corresponding to the Western Pacific (phases 6–7), America and Africa (phases 8–1), Indian Ocean (phases 2–3) and Maritime Continent (phases 4–5).

3 Results and discussions

3.1 Extreme rainfall case of 2019

In the course of an extreme event between 28–31 January 2019, up to 20 mm of rainfall accumulated in some regions of the hyperarid core of the Atacama Desert (<2000 m ASL, Fig. 1b), mainly between 0–12 Local Time (LT, Fig. 1c). These amounts are considered extreme compared to the summer mean long-term precipitation. For example, the stations around Arica recorded up to 3 mm, exceeding ∼6 times the long-term summer average for this location. The stations with the highest accumulated rainfall in the hyperarid core reached 15-20 mm (Tacna and Sierra Gorda), exceeding 5–10 times the long-term average. On the eastern margin of the Atacama (Precordillera, 2000–3500 m ASL) as well as in the Altiplano (>3500 m ASL), rainfall accumulated up to 50 mm (Fig. 1b) with daily peaks around 18 LT and between 00–09 LT (Fig. 1c). This event shows significant rainfall spatial variability across the region, with the lowest values near the coast and increasing to higher lands (Fig. 1b).

We investigate the environmental conditions for Iquique (20.5°S) from ground-based measurements (HATPRO) and ERA5. Both time series show a good agreement in magnitude and variability during the second half of January (Fig. 2a), consistent with the validation performed between March 2019-March 2020 by Vicencio Veloso et al. (2024). In particular, the increase at the end of January of the ERA5 TCWV agrees with the HATPRO retrievals (from 30 to 55 kg m^{-2}), exceeding the 90th percentile of the reanalysis climatology. Moisture increases over most of the troposphere, but the lower free troposphere (900–800 hPa) shows the strongest signal (Fig. S2). At 850 hPa, the specific humidity increased from 3-6 g kg^{-1} before the rain event to almost 12 g kg^{-1} during the event (Fig. 2a). These values are also extreme when compared to the climatology.

The synoptic pattern responsible for the extreme coastal TCWV values is characterized by a southward displaced Bolivian High (BH) positioned east of the Atacama (23°S, 77°W) and a trough over the Southeast Pacific (Fig. 2b). A field of strong poleward-directed winds forms between these upper-level systems, resulting in divergence at its left entrance. This, in turn, supported cyclogenesis in the lower free troposphere starting on 26 January, resulting in a cyclonic circulation in 850 hPa offshore the Atacama Desert and enhanced moisture transport along the west coast of South America from the Tropical Pacific in the lower free troposphere (Fig. 2b, Fig. S3).

After arriving offshore the Atacama coast, the moisture-enriched free-tropospheric air is transported inland and upslope due to the diurnal circulation induced by the surface warming of the west slope of the Andes via the Rutllant Cell. Both stations and WRF show a strong diurnal cycle in the zonal moisture flux, peaking in the afternoon (∼18 LT) and decreasing with elevation more inland (Fig. S4). During the rainfall episode, specific humidity increases from 6 to 12 g kg^{-1} at the lowermost stations and from 5 to 10 g kg^{-1} in precordillera. These values are similar to the specific humidity observed at 850 hPa offshore Iquique. Additionally, lower troposphere stability (LTS) weakens offshore Atacama (Fig. 2c), which could allow a more efficient mixing between the MBL and the free troposphere and further increase the transport of coastal moisture towards the interior of the desert that is usually blocked by the strong inversion at ∼1 km ASL. As a result, the Atacama Desert experiences increasing moisture near the surface, which is decisive to cloud formation and rain.

To further understand how moisture transport interacts with local circulation and topography, we focus on the 72 hours between 28 January 12 LT and 31 January 12 LT with surface weather stations (Fig. S4), satellite (Fig. S5), and high-resolution WRF sim-

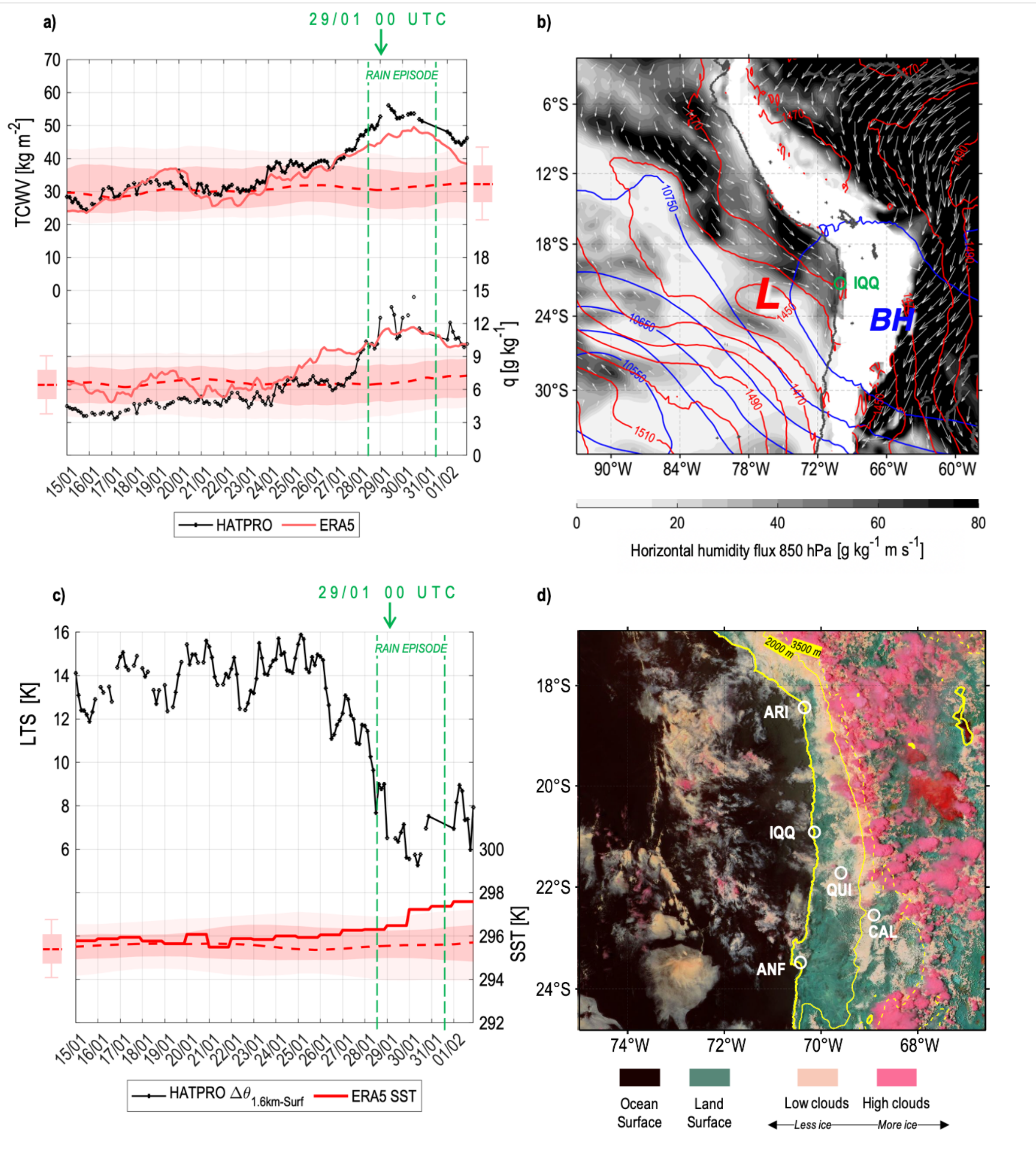

Figure 2. Three-hourly time series of (a) TCWV and specific humidity in 850 hPa, and (c) low troposphere stability (LTS, potential temperature difference between 1.6 km ASL and surface) and SST. Data are shown for HATPRO retrievals (black dotted line) from Iquique Airport (see IQQ location in panel b) and for ERA5 for the average of the four nearest grid points to Iquique (red line). For the SST, the four closest ocean grid points from ERA5 were used. ERA5 climatological (1991–2020) information is provided as a boxplot for the interquartile range, and the upper/bottom whiskers are the 10th/90th percentile, respectively, smoothed with a 30-day window average. (b) 850 hPa humidity flux (shaded color and white arrows above 30 g kg^{-1} m s^{-1}), 850 hPa geopotential height (red lines, every 10 m) and 250 hPa geopotential height (blue lines, every 50 m) on 29 January 2019 00 UTC from ERA5. The location of the Bolivian high (BH) and 850 hPa low pressure (L) are indicated. The Andes cordillera is patched white for altitudes above 850 hPa. (d) Cloud snow-ice product (Bands M3-I3-M11) from NOAA-20/VIIRS at 19:03 UTC (15:03 LT) 29 January 2019 (https://worldview.earthdata.nasa.gov). Yellow lines represent the coastline and terrain altitude at 2000 and 3500 m ASL. The main weather stations used are also shown in white circles.

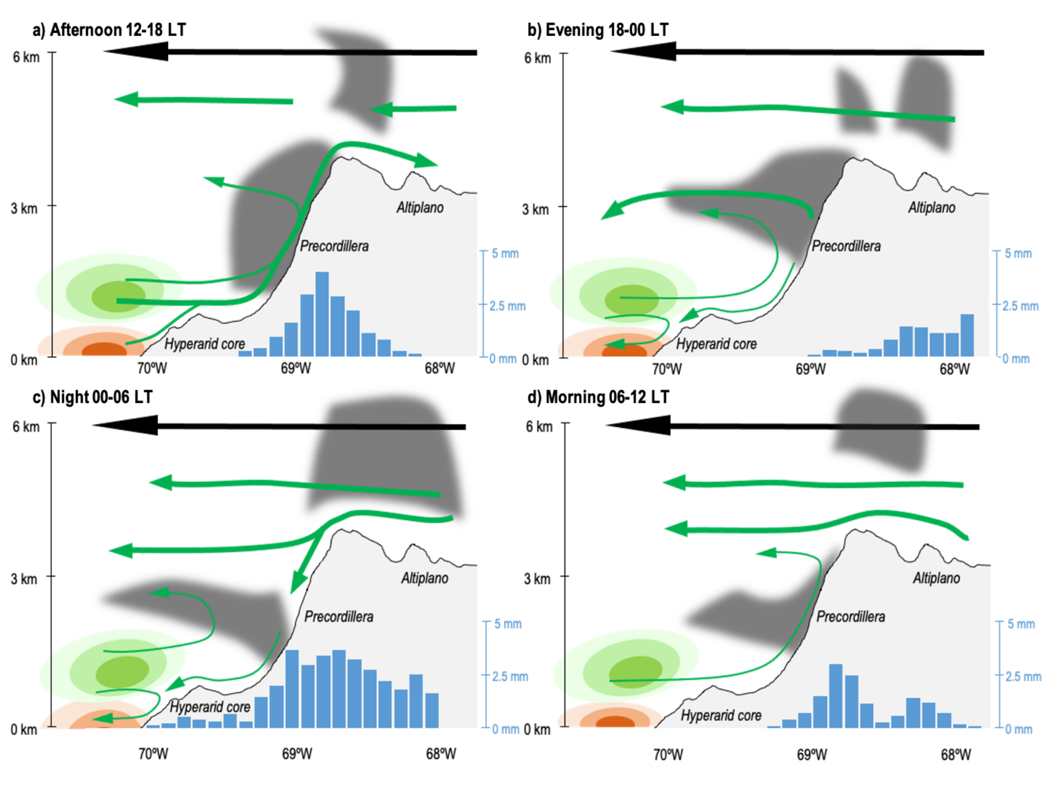

Figure 3. Schematic figure of a cross-section over the Atacama Desert between 18-22°S and 71-68°W for the 2019 extreme rainfall event. Meridional moisture transport from the north and south is shown in green and orange ovals, respectively. Zonal humidity flux is presented in green arrows. In black, the predominant easterly upper troposphere wind is given. Clouds are shown in gray. Rainfall is presented in blue bars (mm 6 hr^{-1}). Four-time segments: (a) afternoon (12-18 LT), (b) evening (18-00 LT), (c) night (00-06 LT), and morning (06-12 LT).

ulation (Fig. S6). We summarize our findings in the schematic Figure 3. In the afternoon (12-18 LT, Fig. 3a), the Andean pumping peaks in westerly moisture transport from the lower free troposphere offshore Atacama towards the Andes. The forced topographic uplift leads to cloud formation along the hyperarid core, identified as low clouds (mainly stratus clouds). In the Precordillera, the stratiform cloud is also observed but with some cumulonimbus embedded (Fig. 2d, Fig. S5), explaining the enhanced rainfall peak at around 18 LT observed at the weather stations (Fig. 1c). Westerly moisture reaches the Altiplano as far east as 68°W, triggering storms in this region as well (Fig. 3a).

In the evening (18-00 LT, Fig. 3b), the return circulation at 3 km ASL is now coupled with the mid-upper tropospheric easterlies, further inducing cloud development closer to the coast. Easterly winds intensify at night (00-06 LT, Fig. 3c), and the lower tropospheric circulation over the Atacama weakens. Nevertheless, stratiform clouds continue to form over the desert and are displaced towards the west, producing the strongest period of precipitation in the hyperarid core, according to the measurements. Additionally, a descending branch of moisture is observed across the precordillera, potentially inducing rain spillover from Altiplano storms. This pattern is present until the next morning (06-12 LT, Fig. 3d) when the radiative heating of the surface again initiates the westerly moisture flux from the Pacific to the Andes, further inducing cloud formation in the Precordillera.

Our results strongly suggest that this rainfall episode is triggered by moisture coming from the Pacific Ocean transported by moist northerlies in the lower free troposphere, as opposed to the more common Amazonian source connected with easterly winds in the mid-upper troposphere. Further evidence supporting this conclusion can be found in Welp et al. (2022), who measured stable water isotopes at Arequipa (16.3°N, 71.5°W, at 2300 m ASL, Fig. 1b). They found isotopically depleted rain during the period from 31 January 2019 to 14 February 2019 (i.e., the same rainfall event of our study), indicating a predominance of oceanic originated precipitation rather than a continental source. We suspect that these results are also valid for the Atacama, which, although located about 200 km south of Arequipa, is affected by the same low-level synoptic pattern. Furthermore, we found evidence that the Rutllant Cell can transport high humidity levels toward the Atacama when the free-troposphere offshore is moist. This complements the findings of Schween et al. (2020), who described a net moisture transport to the east during daytime between 2017-2019 derived from the CRC1211 weather stations network.

3.2 Composite analysis and teleconnections

Given the strong impact of the case analyzed in Section 3.1, we now want to understand how frequently such cases occur and what their driving mechanisms are. We use the 96 rainfall days identified in the hyperarid core identified from 1960–2020 (see Section 2.1) and group them by similar synoptic characteristics. Most of the rainy days (72 cases, ∼75%) have in common a well-developed Bolivian high to the east of the Atacama and an offshore low-pressure at 850 hPa, which induces moisture transport from the north along the southeast Pacific, consistent with the 2019 study case. Based on the strong moisture transport, we refer to these cases as Moist Northerlies (MNs). Another group of rainy days is characterized by a southward displaced BH but without the low-pressure offshore Atacama in the lower free troposphere. Here, rainfall over the Altiplano is likely spilled over the Andean mountain range (9 cases, ∼9%). The rest of the rainy days (15 cases, ∼15%) show a mid-upper tropospheric trough (TT) or a cut-off low (COL) approaching from the west, inducing large-scale instability and moisture transport to the Atacama.

The number of rainfall days and summer accumulated precipitation associated with each mechanism show large interannual variability (Fig. 4a,b). The MN episodes have a higher recurrence between 1987-1991, 2000-2006, and 2018-2020. In fact, the summer of 2020 shows the highest number of days with precipitation so far (10 days), all associated with MNs. The increase in MN rainfall days is mainly driven by Arica, which observes a significant growth in the number of days and rainfall associated with MNs in the decade 2011-2020 compared to the 60s and 70s (Fig. 4c,d). Summer rainfall in Quillagua has only been observed recently, for which MNs account for 6 rainfall days between 2001–2020. In Calama, the MNs peaked in the decades of 1971–1980 and 2001–2020, with 8 episodes per summer, each accounting for between 16–20 mm. In the southern part of the study area, Antofagasta, MNs peaked in duration and intensity in the 1970s (3 days and ∼7 mm), but have not been observed since (Fig. 4c,d).

While the MNs account for 65% of the total rainfall, they are not associated with the most extreme precipitation cases (such as the COLs in 2015, Fig. 4b,d), but they are more recurrent from year to year, becoming the most reliable water source in the hyperarid core. The sub-daily distribution of rainfall intensity for Arica, Antofagasta, and Calama (stations with sub-daily rainfall available) also shows that the MNs are usually associated with light rain (<3.0 mm in 6 hr, Fig. 4e), and often occur during the night (Fig. 4f) in agreement with the 2019 case study. The COL, despite being responsible only for 11% of the rainy days (Fig. 4a), accounts for 25% of the precipitation (Fig. 4b) and higher sub-daily intensity (Fig. 4e).

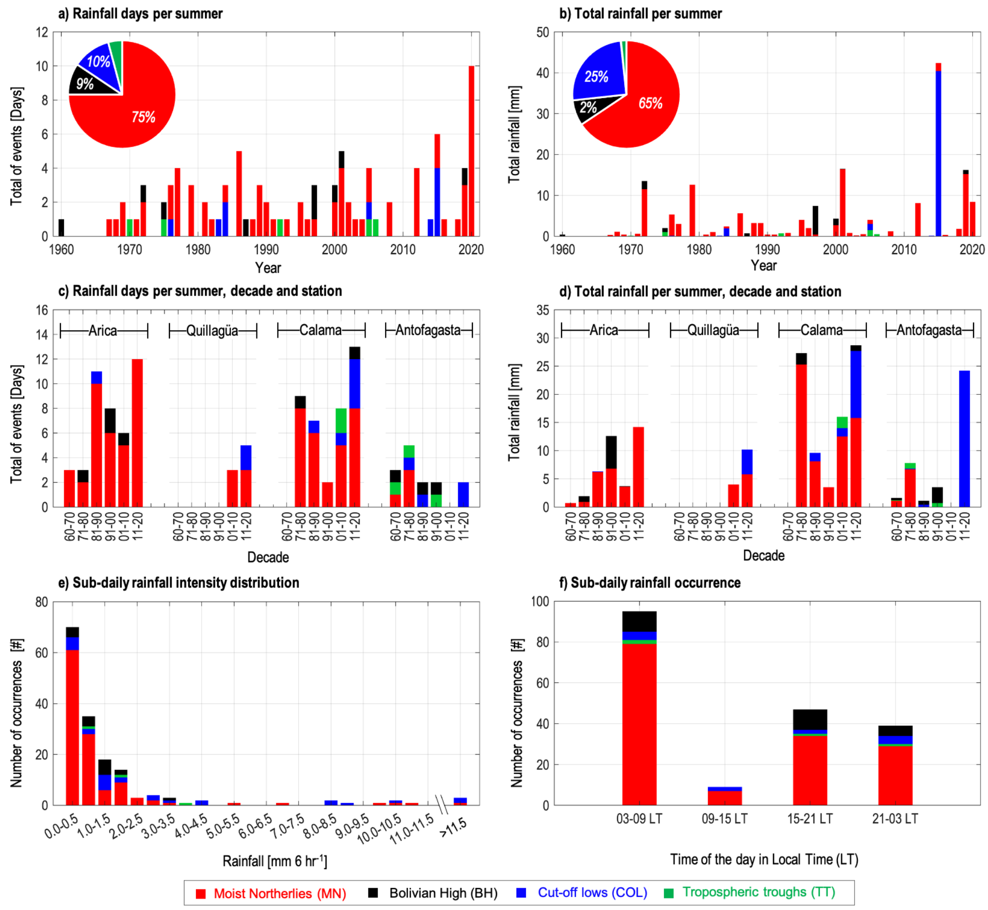

Figure 4. Top: time series of the (a) number of rainy days per summer and (b) total precipitation between 1960–2020, identified from the four weather stations with long-term observations. Middle: decadal (a) rainfall days per summer and (b) total rainfall per summer, divided in the four weather stations used (Arica, Iquique, Calama, and Antofagasta). Bottom: sub-daily distribution of (e) rainfall intensity (mm 6 hr^{-1}) and (f) period of rainfall occurrence. The calculation was made for standard periods of 6 hours (i.e., 03-09 LT, 09-15 LT, 15-21 LT and 21-03 LT). This subdaily rainfall data is only available for Arica, Calama, and Antofagasta weather stations for the period 1964–2020. The type of synoptic configuration is identified by colored bars: red for Moist Northerlies (MN), black for the Bolivian High (BH), green for Cut-off Lows (COL), and blue for Tropospheric Troughs (TT).

The spatial variability of the rainfall associated with MNs reveals that they rarely affect the city of Antofagasta, in which only 29% of the precipitation days have been caused by this mechanism (4 days out of 14). The proportion of rainfall explained by the MNs increases toward the north and east, reaching 74% in Calama (29 days out of 39), 75% in Quillagua (6 days out of 8), and 88% in Arica (38 days out of 43). We suspect that a short distance between the coast and the Andes is crucial to allow the nighttime clouds and precipitation to reach the shoreline. While in Antofagasta, this distance is ∼200 km, in Arica is roughly 60 km. However, a lack of more weather stations prevents further analyses. To link these rainfall characteristics to the typical synoptic conditions, we investigate the composite means and anomalies of the atmospheric state for the identified MN cases in the following.

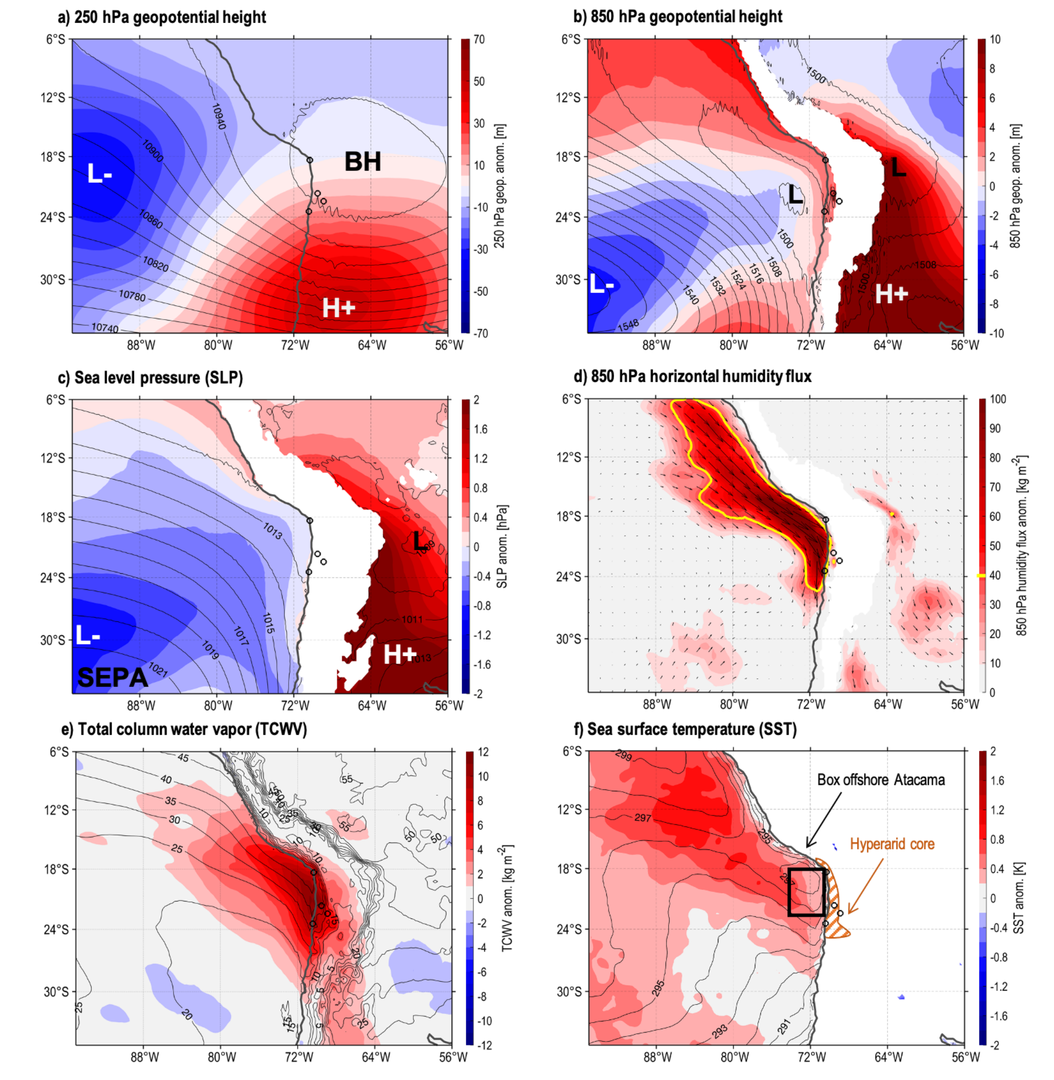

Figure 5. Composite of MN rainfall days (N = 72) of the mean of the MN days (black contours) and the mean anomaly of MN days (shaded colors). The anomalies were computed as the difference between each rainfall day and its respective climatological average (1991–2020) for that specific day for: (a) the 250 hPa geopotential height (in m), (b) 850 hPa geopotential height (in m), (c) Sea level pressure (SLP, in hPa), (d) 850 hPa humidity flux (in g kg^{-1} m s^{-1}), (e) TCWV (in kg m^{-2}), and (f) SST (in K). Low and high-pressure locations are shown in black for the mean and white for anomalies, including the SEPA and BH. Black circles show the location of the four main weather stations for identifying rain events. In panels b, c, and d, the Andes cordillera is patched white for altitudes above 850 hPa. In panel e), the hyperarid core is shown in the orange patch, and the Atacama offshore region (18-23°S, 74-71°W) is shown in the black box.

The MNs composite, derived from ERA5, shows a southward displaced BH, expressed through a strong 250 hPa ridge anomaly over the central Andes (33°S, 69°W, Fig. 5a). Concurrently, a trough anomaly is formed to the west of the BH over the southeastern Pacific (18°S, 95°W). The upper-troposphere anomaly dipole is likely conducive to influencing the lower levels of the troposphere and forming the 850 hPa low-pressure offshore Atacama and a retreat to the south of the Southeast Pacific Anticyclone (SEPA, Fig. 5b). The low pressure is not projected at the surface, and the SEPA dominates the composite. Nevertheless, we observe a generalized weakening of the anticyclone over the Southeast Pacific (Fig. 5c). The weakened SEPA and the 850 hPa low pressure during MN episodes produce weaker moisture transport from the south within the MBL and stronger than normal moisture transport from the north in most of the free troposphere, especially between 900–700 hPa in a box offshore Atacama (18-23°S, 74-70°W, Fig. 6).

Similar moisture transport structures in the free troposphere have been described by Böhm et al. (2021), who used the term MCB. The MCBs detection algorithm is based on the Guan and Waliser (2015) Atmospheric River (AR) catalog, for which ARs are identified according to a percentile threshold regarding integrated water vapor transport (IVT) together with shape criteria. This identification might not be sensitive to the MN discussed here, for which enhanced northerly moisture transport is limited to the lower free troposphere over a depth of ∼200 hPa (Fig. 6). This moisture transport is insufficient to produce an outstanding IVT signal, given that moist southerlies in the MBL are still present during the MN episodes, counteracting the integrated moisture transport. This explains why, from the 15 summer MCBs found by Böhm et al. (2021) between 1979–2019, none correspond to MN episodes identified in this study. Nevertheless, the horizontal moisture transport structure of the MNs resembles an AR in the lower free troposphere (∼850 hPa, Fig. 5d), bringing enough humidity to produce above-normal TCWV anomalies offshore Atacama (Fig. 5e).

Warmer than normal SST has been acknowledged as a significant factor in precipitation events in the Atacama, primarily by enhancing humidity and instability (Bozkurt et al., 2016). During MN episodes, SST increases in the Southeast Pacific, with anomalies up to +1 K (Fig. 5f). However, we suspect that this warming is the consequence of the MN synoptic pattern expressed with the overall weakening of the SEPA (Fig. 5c) and reduced southerly winds at the surface, which lower the transport of cold waters from the south and hinder coastal upwelling. Additionally, warmer SST during MN episodes is typically confined to the coastal areas and coincides with neutral (∼35%) or weak La Niña conditions (∼38%) in the Central Pacific (Fig. 7a), and with mainly neutral conditions in El Niño 1+2 (∼69%, Fig. 7a). Thus, it is suspected that the observed warming offshore Perú and northern Chile during MN episodes is predominantly influenced by changes in atmospheric circulation rather than being the primary cause of the MN pattern and the associated precipitation.

Furthermore, the relationship between La Niña in the Central Pacific and MNs can be partially explained by the weakening of the subtropical jet due to the reduction of the meridional temperature gradient between the tropics and mid-latitudes. A weaker jet stream allows the anomalous southward displacement of the BH (Garreaud et al., 2003), enhancing the formation of the 850 hPa low-pressure offshore the Atacama and weakening the SEPA. A similar impact can result from the active phases of MJO. For the period 1979–2020 (period of data availability of the index), most of the MN cases are related to phases 7, 8, and 1 (∼40%, Fig. 7b). These phases are associated with summer heatwaves in central Chile (32-38°S, Jacques-Coper et al., 2021; Demortier et al., 2021) due to a synoptic configuration over the Pacific and South America analogous to the MN composite, i.e., an exacerbated strong ridge anomaly over the central Andes accompanied by a trough anomaly over the Southeast Pacific. This upper-troposphere pattern can also contribute to displacing the BH and the SEPA poleward, further helping to form the 850 hPa low-pressure offshore Atacama. An example of this compound event was

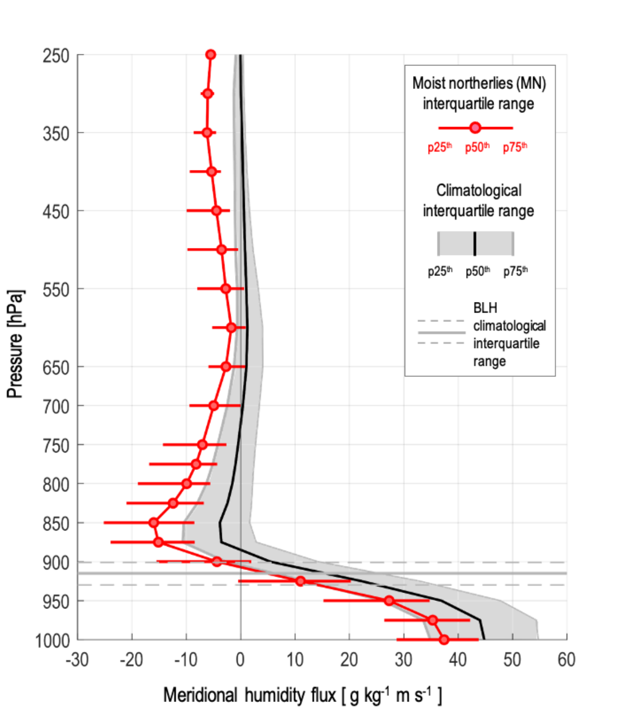

Figure 6. Vertical profile of the meridional humidity flux (red dotted line) for a box offshore Atacama (18-23°S, 74-71°W). The interquartile range for the 72 MN episodes is shown in a red horizontal line, and the summer climatology for the 1991-2020 period is in the gray-shaded polygon. The boundary layer height (BLH) interquartile range climatology is shown in the gray horizontal lines. Data from ERA5.

observed during the January 2019 study case, in which several cities south of 33°S recorded record heat a few days before the extreme rainfall event in the Atacama (Jacques-Coper et al., 2021). Yet, around 37% of the MN days still occur in the inactive phase of the MJO (Fig. 7b).

3.3 Long-term trends and impacts of MNs

Given the importance of MNs in supplying moisture to the Atacama, the question arises whether their frequency is affected by global climate change. The summer-averaged TCWV for a box offshore Atacama (18-23°S, 74-71°W) shows a positive trend, especially evident in the periods starting between 1970-1998 and ending between 2018-2020, ranging from 0.7 to 1.6 kg m^{-2} decade^{-1} (Fig. 8a). These changes in the summer mean are also observed in the daily means of TCWV (Fig. 8c). The probability distribution shows that the upper-right tail extends to higher values during the 2011-2020 period compared to previous decades, with the maximum values shifting from 45 to 55 kg m^{-2}. The change in the distribution also includes a shift from an unimodal to a bimodal distribution in TCWV, e.g., a secondary mode around 40 kg m^{-2} appears in the 2011–2020 distribution (Fig. 8c).

The increase in TCWV observed in the box offshore Atacama is part of a regional pattern in the Southeast Pacific. Taking the period 1991–2020, the mean TCWV trend reaches up to 2 kg m^{-2} decade^{-1} and is significant at the 95% confidence level offshore Peru and northern Chile (Fig. 9a). The 90th percentile of summer TCWV shows a sim-

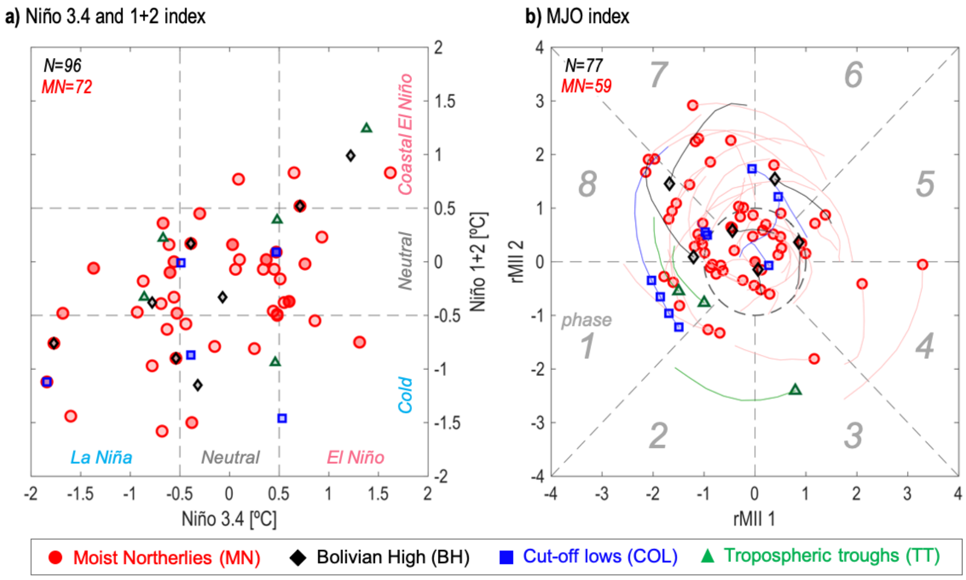

Figure 7. (a) Scatter plot of monthly SST anomalies for Niño 3.4 (x-axis) and Niño 1+2 (y-axis) for each summer rainfall day in the Atacama Desert between 1960–2020, and (b) MJO index (Wang et al., 2022) for each summer rainfall day in the Atacama Desert between 1979–2020. It includes the previous 7-day MJO phase (thin line). In both panels, the color and shape of the symbol represent the type of rainfall mechanism identified: red circle for moist northerlies (MN), black diamonds for the Bolivian High (BH), green triangles for cut-off lows (COL), and blue squares for tropospheric troughs (TT). In the upper left corner, the number of rainy days (N) and the number of rainy days associated with MN are shown.

ilar spatial pattern, but almost doubles the trend of the mean, reaching up to 3 kg m^{-2} decade^{-1} near the Atacama coast (Fig. 9b).

The positive TCWV trend results from a general increase in moisture throughout most of the free troposphere and is most prominent in its lower levels (800-900 hPa, Fig. 10a). We attribute this trend to the rising frequency of the MN condition, this is, a decline in the 850 hPa geopotential height offshore Atacama (Fig. 9c) that reinforces northerly winds along the western coast of South America due to increased zonal pressured gradient (Fig. 10b), enhancing moisture transport from the tropics in the lower free troposphere and leading to a positive trend in specific humidity at 850 hPa (Fig. 9d). The warm trend in the SST offshore Atacama is spatially much more limited (Fig. 9e) than the general increase in TCWV. We suspect that this trend is potentially moistening the MBL (Fig. 10a), although other factors may play a role (e.g., weaker southerly winds, Fig. 10b).

The negative trend in the form of the 850 hPa low-pressure off the coast of Atacama is a somewhat curious feature, considering that most of the subtropical and mid-latitude regions exhibit a marked positive trend in the geopotential height and sea level pressure as a consequence of global warming (Fig. 9c,f, and e.g., Gillett & Stott, 2009). However, we suspect that both factors are linked. The poleward displacement of the subtropical jet due to the Hadley cell expansion (Lu et al., 2007) allows a more frequent formation of the BH in the upper troposphere at the synoptic scale as proposed by Garreaud

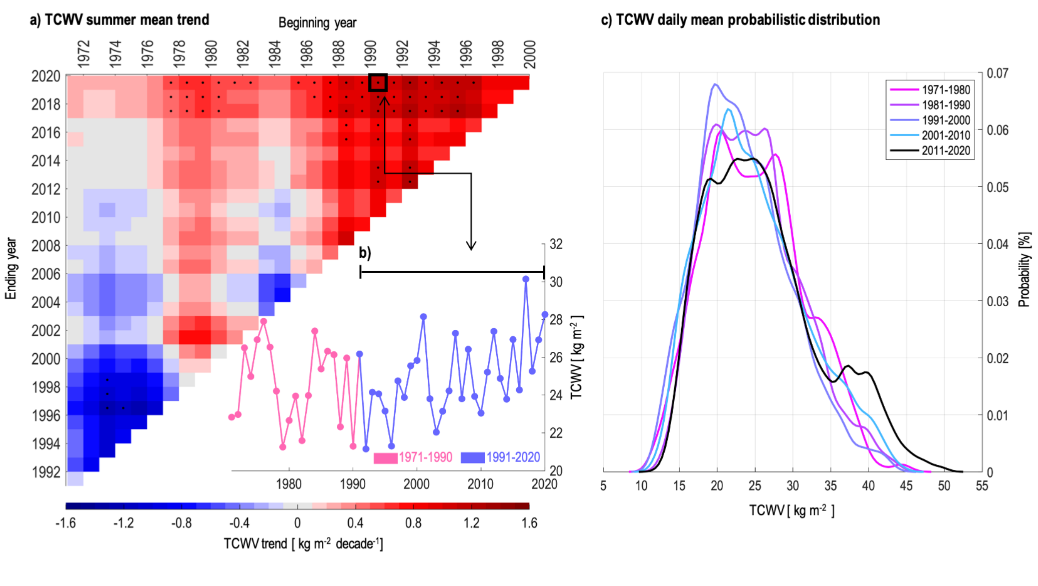

Figure 8. (a) Heatmap of the multi-trend analysis of TCWV summer mean (December–March) for a box offshore Atacama (18-23°S, 74-71°W) for different periods starting in 1971 and ending in 2020. Significance at 95% is marked with a black dot in the center of the box. (b) Time series of summer TCWV from 1971–2020 averaged for the same box offshore Atacama. The blue time series corresponds to the period 1991–2020, highlighted in the heatmap with a black square. (c) The probability density of daily means of summer TCWV in the same Atacama offshore region for different decades (colored lines). TCWV is obtained from ERA5.

(1999). As discussed in the previous section, the anomalous poleward displaced BH is conducive to forming the 850 hPa low-pressure offshore Atacama.

Additionally, the expansion of the Hadley cell results in a shift of the SEPA towards the pole, relaxing the pressure gradient along the west coast of South America and potentially helping the low pressure to form. The tropical expansion has been linked to global warming induced by greenhouse gases (GHG) forcing (Lu et al., 2007), but other factors may also play a role. For example, the positive trend in the Southern Annular Mode (SAM, Marshall, 2003), in which the polar jet weakens and displaced poleward, especially in austral summer (Fogt & Marshall, 2020), help to displace the southern edge of the SEPA poleward. This trend is partially linked to the stratospheric ozone loss, with GHG and tropical variability playing secondary roles (Fogt & Marshall, 2020). Therefore, it is highly likely that the observed trend in moisture and circulation along the west coast of South America results from several processes occurring at different time scales, conspiring to produce a generalized increase in humidity transport to the Atacama Desert.

The MN episodes were identified in this study using a set of four weather stations located in the hyperarid core. Nevertheless, we suspect that the MN can have an influence beyond this region. As few precipitation measurements exist in the Atacama, the presence of vegetation could serve as an indirect proxy for past changes in the rainfall regime. For example, the blooming desert or "desierto florido" is frequently observed in Southern Atacama (25-30°S) and is a good tracer of winter rainfall episodes. Similarly, Chávez et al. (2019) found the first evidence of a "pre-Altiplanic blooming desert", triggered by an anomalous wet summer in 2012 in the precordillera. This anomalous blooming was only observed recently despite research spanning from 1981 to 2015. This aligns well with a wet year in the hyperarid core with at least four rainy days related to MNs

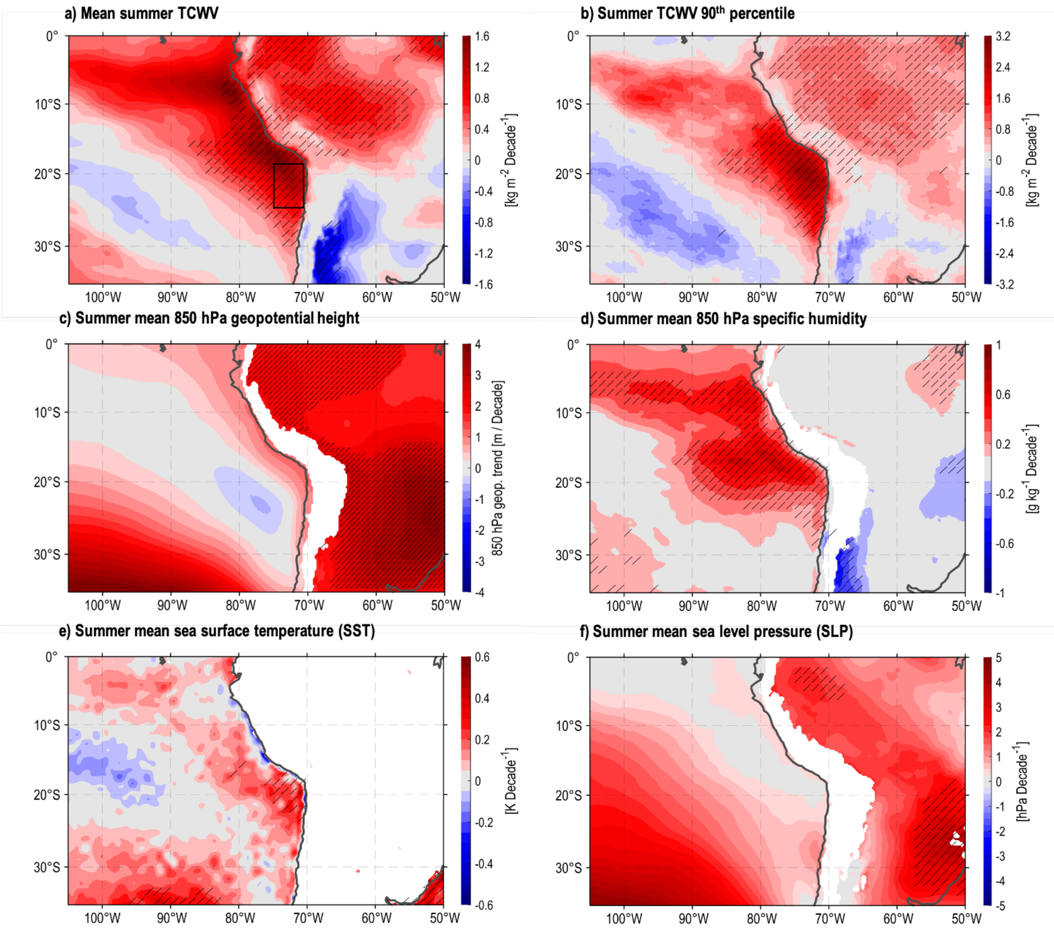

Figure 9. Linear trend (1991-2020) for summer (December-March) of (a) mean TCWV, (b) summer 90^{th} percentile, (c) mean 850 hPa geopotential height, (d) mean 850 hPa specific humidity, (e) mean SST and (f) sea level pressure. Areas with black stripes indicate statistical significance of 95% of confidence level. In panels c, d, e, and f, the Andes cordillera is patched white for altitudes above 850 hPa. Data from ERA5.

(Fig.4a). The blooming seems to be part of a greater greening pattern affecting eastern Atacama. Lepage et al. (2023) found a marked positive trend of the normalized difference vegetation index (NDVI) between 2000–2020 in a greening strip between Southern Perú and Northern Chile (7.5–22.5°S). As the greening is so extended, it is unlikely to be linked to land-use changes. We propose that the more frequent MN mechanism offshore Atacama observed in the last decades complements the classic easterly moisture source for summer storms, increasing moisture availability on the eastern edge of the Atacama and the precordillera, and inducing more frequent precipitation. The increased moisture advected from the coast into the desert matches with recent estimations of relatively high fog frequency in the precordillera (Böhm et al., 2021), which could further provide water to vegetation.

4 Summary and conclusions

We have investigated summer rainfall episodes in the Atacama Desert using a case study and a composite analysis from reanalysis ERA5, high-resolution WRF simulations,

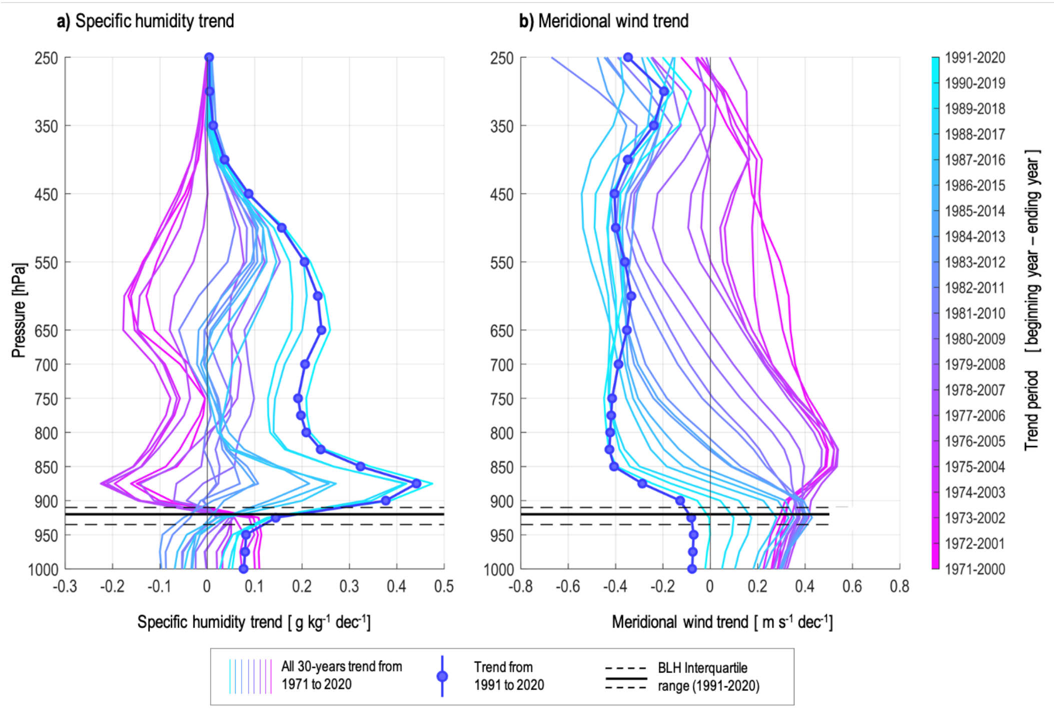

Figure 10. Vertical profiles of austral summer of (a) specific humidity trend and (b) meridional wind linear trend for 30 years period (colored lines) for the Atacama offshore region (18-23°S, 74-71°W). The blue dotted line corresponds to the 1991–2020 trend. We included the interquartile range of the boundary layer height (BLH, dashed thin black line) and the mean (thick black line) for the period 1991–2020. Data from ERA5.

surface observations, satellites, and remote sensing. Around 75% of rainfall days and 65% of total rainfall in summer in the hyperarid core of the Atacama are triggered by moisture coming from the Pacific. We called these episodes Moist Northerlies (MNs), associated with an anomalous southward displaced BH and a trough anomaly in the upper troposphere over the southeast Pacific. This upper-troposphere dipole is conducive to forming a non-frontal low-pressure system at 850 hPa offshore Perú and northern Chile. In the forefront of the low pressure, an atmospheric river-like structure transports the moisture from the tropical eastern Pacific to the south. This produces a marked increase in TCWV offshore Atacama, reaching extreme values (up to ∼55 kg m^{-2}) that are typically observed over the Amazon basin.

Based on a case study, we found that the classic Rutllant Cell that brings dry air from the subsidence region along the west coast of South America to the Andes is also a moist circulation, pumping the moisture-enriched air from the lower free-troposphere offshore Atacama to the interior. Surface-specific humidity can increase from 3 to 12 g kg^{-1} in the hyperid core and precordillera during the rainfall episode. The topographic uplift triggers clouds along the precordillera, mainly as stratus clouds but with some cumulonimbus embedded. Part of the moisture can reach the Altiplano and serve as a source for the evening thunderstorms. Mid-troposphere easterly winds at night bring clouds to the pampas and the coast. Evidence from 72 rainfall episodes in the Atacama shows that this mechanism produces mainly light rain during the night (03-09 LT), although rain can occur at any time of the day. The MNs affect mostly the northern part of the desert (i.e., Arica), the east (i.e., Quillagua and Calama), and decrease its influence to the south (i.e., Antofagasta).

Most of the MN rainfall episodes occur during the neutral or weak La Niña conditions in the Central Pacific, and during the phases 7-8-1 of the MJO. These large-scale oscillations are conducive to weakening the subtropical jet and producing the upper-troposphere dipole over the Southeast Pacific that is required to form the 850 hPa low-pressure system. Our results suggest that this mechanism is driven mainly by atmospheric dynamics and not by changes in local SST offshore Atacama. In fact, warmer than normal SST anomalies over the Southeast Pacific accompanying the MN episodes seem to be a consequence of the general weakening of the SEPA rather than a triggering mechanism of the MNs and the precipitation.

Finally, a trend analysis highlights that the MNs have become more frequent within the last ∼30 years, further enhancing extreme values of TCWV offshore Atacama. This extra moisture supply explains the increase in MN rainfall episodes in the last decades in the northern and eastern Atacama, the general wet trend across much of southern Perú and Northern Chile, and the greening in the precordillera. Further measurements are needed to correctly understand how Pacific-originate westerly moisture is transported inland, considering the region's complex topography. Future works must address the impact of the Hadley cell expansion, GHG, and SAM on the MN rainfall mechanism accurately. For example, statistically downscaled climate projections show increased summer rainfall in the Atacama under different future global warming scenarios (Araya-Osses et al., 2020). We suspect that this increased summer rainfall could be influenced by enhanced MN configuration. Furthermore, wetter conditions during globally warmer climates in the past (e.g., Holocene and Pleistocene) have mainly been linked to enhanced periods of El Niño in the Equatorial Pacific and its impact on winter rainfall (Ritter et al., 2019; González-Pinilla et al., 2021) may also be partially influenced by the rising frequency of MN episodes in summer, a neutral-cold ENSO induced mechanism.

Open Research Section

ERA5 data (Hersbach et al., 2020) were downloaded from the Copernicus Climate Data Store (CDS) via `https://cds.climate.copernicus.eu/`. Data from WRF simulation can be obtained from the CRC1211 database via `https://www.crc1211db.uni-koeln.de/`. Rainfall data was obtained via: (1) CR2, `http://www.cr2.cl/datos-de-precipitacion/`, (2) DMC, `https://climatologia.meteochile.gob.cl` and (3) DGA, `https://dga.mop.gob.cl`. ENSO index can be downloaded via `https://www.cpc.ncep.noaa.gov/data/indices`. MJO index can be downloaded via `https://www.psl.noaa.gov/mjo/mjoindex/`. We acknowledge the use of imagery from the NASA Worldview application (`https://worldview.earthdata.nasa.gov`), part of the NASA Earth Observing System Data and Information System (EOSDIS).

Acknowledgments

We gratefully acknowledge financial support by the Deutsche Forschungsgemeinschaft (DFG, German Research Foundation)–Projektnummer 268236062-SFB 1211.

References

Araya-Osses, D., Casanueva, A., Román-Figueroa, C., Uribe, J. M., & Paneque, M. (2020). Climate change projections of temperature and precipitation in Chile based on statistical downscaling. *Climate Dynamics*, *54*, 4309–4330. doi: https://doi.org/10.1007/s00382-020-05231-4

Barrett, B., Campos, D., Vicencio, J., & Rondanelli, R. (2016). Extreme temperature and precipitation events in March 2015 in central and northern Chile.

Journal of Geophysical Research: Atmospheres, *121*(9), 4563–4580.

Böhm, C., Schween, J. H., Reyers, M., Maier, B., Löhnert, U., & Crewell, S. (2021). Toward a Climatology of Fog Frequency in the Atacama Desert via Multispectral Satellite Data and Machine Learning Techniques. *Journal of Applied Meteorology and Climatology*, *60*(8), 1149–1169. doi: https://doi.org/10.1175/JAMC-D-20-0208.1

Bozkurt, D., Rondanelli, R., Garreaud, R., & Arriagada, A. (2016). Impact of Warmer Eastern Tropical Pacific SST on the March 2015 Atacama Floods. *Monthly Weather Review*, *144(11)*, 4441-4460.

Böhm, C., Reyers, M., Knarr, L., & Crewell, S. (2021). The role of moisture conveyor belts for precipitation in the Atacama Desert. *Geophysical Research Letters*, *48*(24), e2021GL094372. doi: https://doi.org/10.1029/2021GL094372

Chávez, R., Moreira-Muñoz, A., Galleguillos, M., Olea, M., Aguayo, J., Latín, A., . . . Manríquez, H. (2019). GIMMS NDVI time series reveal the extent, duration, and intensity of "blooming desert" events in the hyper-arid Atacama Desert, Northern Chile. *International Journal of Applied Earth Observation and Geoinformation*, *76*, 193-203. doi: https://doi.org/10.1016/j.jag.2018.11.013

Demortier, A., Bozkurt, D., & Jacques-Coper, M. (2021). Identifying key driving mechanisms of heat waves in central Chile. *Climate Dynamics*, *57*(9-10), 2415–2432. doi: https://doi.org/10.1007/s00382-021-05810-z

Dunai, T. J., Melles, M., Quandt, D., Knief, C., & Amelung, W. (2020). Whitepaper: Earth – evolution at the dry limit. *Global and Planetary Change*, *193*, 103275. doi: https://doi.org/10.1016/j.gloplacha.2020.103275

Fogt, R. L., & Marshall, G. J. (2020). The Southern Annular Mode: variability, trends, and climate impacts across the Southern Hemisphere. *Wiley Interdisciplinary Reviews: Climate Change*, *11*(4), e652. doi: https://doi.org/10.1002/wcc.652

Garreaud, R. (1999). Multiscale Analysis of the Summertime Precipitation over the Central Andes. *Monthly Weather Review*, *127*(5), 901 - 921. doi: https://doi.org/10.1175/1520-0493(1999)127⟨0901:MAOTSP⟩2.0.CO;2

Garreaud, R., & Aceituno, P. (2001). Interannual Rainfall Variability over the South American Altiplano. *Journal of Climate*, *14*(12), 2779 - 2789. doi: https://doi.org/10.1175/1520-0442(2001)014⟨2779:IRVOTS⟩2.0.CO;2

Garreaud, R., Vuille, M., & Clement, A. (2003). The climate of the Altiplano: observed current conditions and mechanisms of past changes. *Palaeogeography, palaeoclimatology, palaeoecology*, *194*(1-3), 5–22.

Gillett, N., & Stott, P. (2009). Attribution of anthropogenic influence on seasonal sea level pressure. *Geophysical Research Letters*, *36*(23). doi: https://doi.org/10.1029/2009GL041269

González-Pinilla, F. J., Latorre, C., Rojas, M., Houston, J., Rocuant, M. I., Maldonado, A., . . . Betancourt, J. L. (2021). High-and low-latitude forcings drive Atacama Desert rainfall variations over the past 16,000 years. *Science Advances*, *7*(38), eabg1333. doi: 10.1126/sciadv.abg1333

Guan, B., & Waliser, D. (2015). Detection of atmospheric rivers: Evaluation and application of an algorithm for global studies. *Journal of Geophysical Research - Atmospheres*, *120(24)*, 12514-12535.

Heidinger, H., Carvalho, L., Jones, C., Posadas, A., & Quiroz, R. (2018). A new assessment in total and extreme rainfall trends over central and southern Peruvian Andes during 1965–2010. *International Journal of Climatology*, *38*, e998–e1015. doi: https://doi.org/10.1002/joc.5427

Hersbach, H., Bell, B., Berrisford, P., Hirahara, S., Horányi, A., Muñoz-Sabater, J., . . . Thépaut, J.-N. (2020). The ERA5 global reanalysis. *Quarterly Journal of the Royal Meteorological Society*, *146*(730), 1999-2049. doi: https://doi.org/10.1002/qj.3803

Hoffmeister, D. (2018). Meteorological and soil measurements of the permanent

weather stations in the Atacama desert, Chile. *CRC1211 Database*. Retrieved from https://www.crc1211db.uni-koeln.de/DOI/doi.php?doiID=1
Houston, J., & Hartley, A. J. (2003). The central Andean west-slope rainshadow and its potential contribution to the origin of hyper-aridity in the Atacama Desert. *International Journal of Climatology*, *23*(12), 1453–1464. doi: 10.1002/joc.938
Huang, B., Thorne, P. W., Banzon, V. F., Boyer, T., Chepurin, G., Lawrimore, J. H., ... Zhang, H.-M. (2017). Extended reconstructed sea surface temperature, version 5 (ERSSTv5): upgrades, validations, and intercomparisons. *Journal of Climate*, *30*(20), 8179–8205.
Jacques-Coper, M., Veloso-Aguila, D., Segura, C., & Valencia, A. (2021). Intraseasonal teleconnections leading to heat waves in central Chile. *International Journal of Climatology*, *41*(9), 4712-4731. doi: https://doi.org/10.1002/joc.7096
Jordan, T. E., Herrera, C., Godfrey, L. V., Colucci, S. J., Gamboa, C., Urrutia, J., ... Paul, J. F. (2019). Isotopic characteristics and paleoclimate implications of the extreme precipitation event of March 2015 in northern Chile. *Andean Geology*, *46*(1), 1–31. doi: https://doi.org/:10.5027/andgeoV46n1-3087
Lepage, H. V., Barnes, E., Kor, E., Hunter, M., & Barnes, C. H. (2023). Greening and Browning Trends on the Pacific Slope of Peru and Northern Chile. *Remote Sensing*, *15*(14), 3628. doi: https://doi.org/10.3390/rs15143628
Lu, J., Vecchi, G. A., & Reichler, T. (2007). Expansion of the Hadley cell under global warming. *Geophysical Research Letters*, *34*(6). doi: https://doi.org/10.1029/2006GL028443
L'Heureux, M. L., Collins, D. C., & Hu, Z.-Z. (2013). Linear trends in sea surface temperature of the tropical Pacific Ocean and implications for the El Niño-Southern Oscillation. *Climate Dynamics*, *40*(5-6), 1223–1236. doi: https://doi.org/10.1007/s00382-012-1331-2
Madden, R., & Julian, P. (1972). Description of global-scale circulation cells in the tropics with a 40–50-day period. *J. Atmos. Sci.*, *29*, 1109-1123. doi: https://doi.org/10.1175/1520-0469(1972)029⟨1109:DOGSCC⟩2.0.CO;2
Marshall, G. J. (2003). Trends in the Southern Annular Mode from observations and reanalyses. *Journal of climate*, *16*(24), 4134–4143. doi: https://doi.org/10.1175/1520-0442(2003)016⟨4134:TITSAM⟩2.0.CO;2
Meseguer-Ruiz, O., Cortesi, N., Guijarro, J. A., & Sarricolea, P. (2020). Weather regimes linked to daily precipitation anomalies in Northern Chile. *Atmospheric Research*, *236*, 104802. doi: https://doi.org/10.1016/j.atmosres.2019.104802
Olivares, M. (2020). Caracterización climatológica de la precipitación en temporada estival en la zona norte de Chile considerando el periodo entre los años 1990 y 2019. *Stratus*, 1-35. Retrieved from https://revistastratus.meteochile.gob.cl/index.php/2020/12/01/caracterizacion-climatologica-de-la-precipitacion-en-temporada-estival-en-la-zona-norte-de-chile-considerando-el-periodo-entre-los-anos-1990-y-2019/
Reyers, M. (2018). *WRF output daily accumulated total precipitation 10 km resolution Atacama* [dataset]. CRC1211 Database (CRC1211DB). Retrieved from https://doi.org.10.5880/CRC1211DB.20
Reyers, M., Böhm, C., Knarr, L., Shao, Y., & Crewell, S. (2020). Synoptic-to-regional scale analysis of rainfall in the Atacama Desert (18S–26S) using a long-term simulation with WRF. *Monthly Weather Review*, *149(1)*, 91-112. doi: https://doi.org/10.1175/MWR-D-20-0038.1
Reyers, M., & Shao, Y. (2019). Cutoff lows off the coast of the Atacama Desert under present day conditions and in the Last Glacial Maximum. *Global and Planetary Change*, *181*, 102983.
Ritter, B., Wennrich, V., Medialdea, A., Brill, D., King, G., Schneiderwind, S., ... others (2019). Climatic fluctuations in the hyperarid core of the At-

acama Desert during the past 215 ka. *Scientific reports*, *9*(1), 5270. doi: https://doi.org/10.1038/s41598-019-41743-8

Rondanelli, R., Hatchett, B., Rutllant, J., Bozkurt, D., & Garreaud, R. (2019). Strongest MJO on record triggers extreme Atacama rainfall and warmth in Antarctica. *Geophysical Research Letters*, *46*(6), 3482–3491. doi: https://doi.org/10.1029/2018GL081475

Rondanelli, R., Molina, A., & Falvey, M. (2015). The Atacama Surface Solar Maximum. *Bulletin of the American Meteorological Society*, *96*(3), 405 - 418. doi: 10.1175/BAMS-D-13-00175.1

Rose, T., Crewell, S., Löhnert, U., & Simmer, C. (2005). A network suitable microwave radiometer for operational monitoring of the cloudy atmosphere. *Atmospheric Research*, *75*(3), 183-200. (CLIWA-NET: Observation and Modelling of Liquid Water Clouds) doi: https://doi.org/10.1016/j.atmosres.2004.12.005

Rutllant, J., Muñoz, R., & Garreaud, R. (2013). Meteorological observations on the northern Chilean coast during VOCALS-REx. *Atmospheric Chemistry and Physics*, *13*(6), 3409–3422.

Schween, J. H., del Rio, C., García, J.-L., Osses, P., Westbrook, S., & Löhnert, U. (2022). Life Cycle of Stratocumulus Clouds over one Year at the Coast of the Atacama Desert. *Atmospheric Chemistry and Physics Discussions*, *2022*, 1–33. doi: 10.5194/acp-2022-108

Schween, J. H., Hoffmeister, D., & Löhnert, U. (2020). Filling the observational gap in the Atacama Desert with a new network of climate stations. *Global and Planetary Change*, *184*, 103034. doi: https://doi.org/10.1016/j.gloplacha.2019.103034

Skamarock, W. C., Klemp, J. B., Dudhia, J., Gill, D. O., Barker, D. M., Duda, M. G., ... others (2008). A description of the advanced research WRF version 3. *NCAR technical note*, *475*, 113.

Valdivielso, S., Vázquez-Suñé, E., & Custodio, E. (2020). Origin and variability of oxygen and hydrogen isotopic composition of precipitation in the Central Andes: A review. *Journal of Hydrology*, *587*, 124899. doi: https://doi.org/10.1016/j.jhydrol.2020.124899

Vicencio, J. (2021). Analysis of an extreme precipitation event in the Atacama Desert on January 2020 and its relationship to humidity advection along the Southeast Pacific. *Atmósfera*, *35*(3), 421-448. doi: https://doi.org/10.20937/ATM.52911

Vicencio Veloso, J., Böhm, C., Schween, J. H., Löhnert, U., & Crewell, S. (2024). A comparative study of the atmospheric water vapor in the Atacama and Namib Desert. *Global and Planetary Change*, *232*, 104320. doi: https://doi.org/10.1016/j.gloplacha.2023.104320

Vuille, M., Hardy, D. R., Braun, C., Keimig, F., & Bradley, R. S. (1998). Atmospheric circulation anomalies associated with 1996/1997 summer precipitation events on Sajama Ice Cap, Bolivia. *Journal of Geophysical Research: Atmospheres*, *103*(D10), 11191–11204.

Wang, S., Martin, Z. K., Sobel, A. H., Tippett, M. K., Dias, J., Kiladis, G. N., ... Wu, J. (2022). A multivariate index for tropical intraseasonal oscillations based on the seasonally-varying modal structures. *Journal of Geophysical Research: Atmospheres*, *127*(4), e2021JD035961. (e2021JD035961 2021JD035961) doi: https://doi.org/10.1029/2021JD035961

Welp, L. R., Olson, E. J., Valdivia, A. L., Larico, J. R., Arhuire, E. P., Paredes, L. M., ... Michalski, G. M. (2022). Reinterpreting Precipitation Stable Water Isotope Variability in the Andean Western Cordillera Due To Sub-Seasonal Moisture Source Changes and Sub-Cloud Evaporation. *Geophysical Research Letters*, *49*(18), e2022GL099876. doi: https://doi.org/10.1029/2022GL099876

Wennrich, V., Böhm, C., Brill, D., Carballeira, R., Hoffmeister, D., Jaeschke, A., ...

Melles, M. (2024). Late Pleistocene to modern precipitation changes at the Paranal clay pan, central Atacama Desert. *Global and Planetary Change*, *233*, 104349. doi: https://doi.org/10.1016/j.gloplacha.2023.104349

Figure 1.

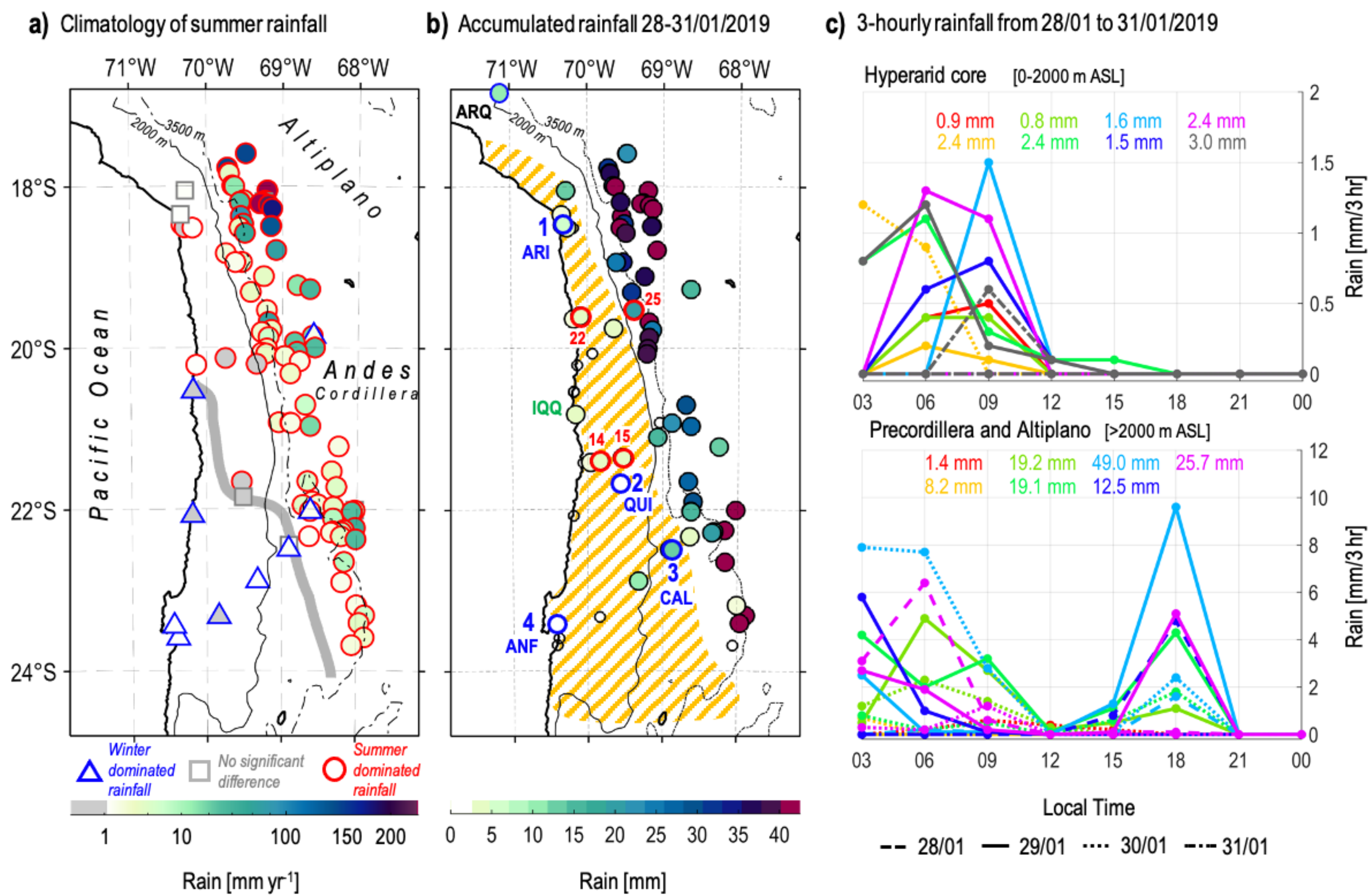

a) Climatology of summer rainfall
b) Accumulated rainfall 28-31/01/2019
c) 3-hourly rainfall from 28/01 to 31/01/2019
71°W
70°W
69°W
68°W
18°S
20°S
22°S
24°S
2000 m
3500 m
Altiplano
Pacific Ocean
Andes
Cordillera
Winter dominated rainfall
No significant difference
Summer dominated rainfall
1
10
100
150
200
Rain [mm yr-1]
ARQ
1
ARI
22
25
IQQ
14
15
2
QUI
3
CAL
4
ANF
0
5
10
15
20
25
30
35
40
Rain [mm]
Hyperarid core [0-2000 m ASL]
0.9 mm
0.8 mm
1.6 mm
2.4 mm
2.4 mm
2.4 mm
1.5 mm
3.0 mm
Rain [mm/3 hr]
Precordillera and Altiplano [>2000 m ASL]
1.4 mm
19.2 mm
49.0 mm
25.7 mm
8.2 mm
19.1 mm
12.5 mm
03
06
09
12
15
18
21
00
Local Time
28/01
29/01
30/01
31/01

Figure 2.

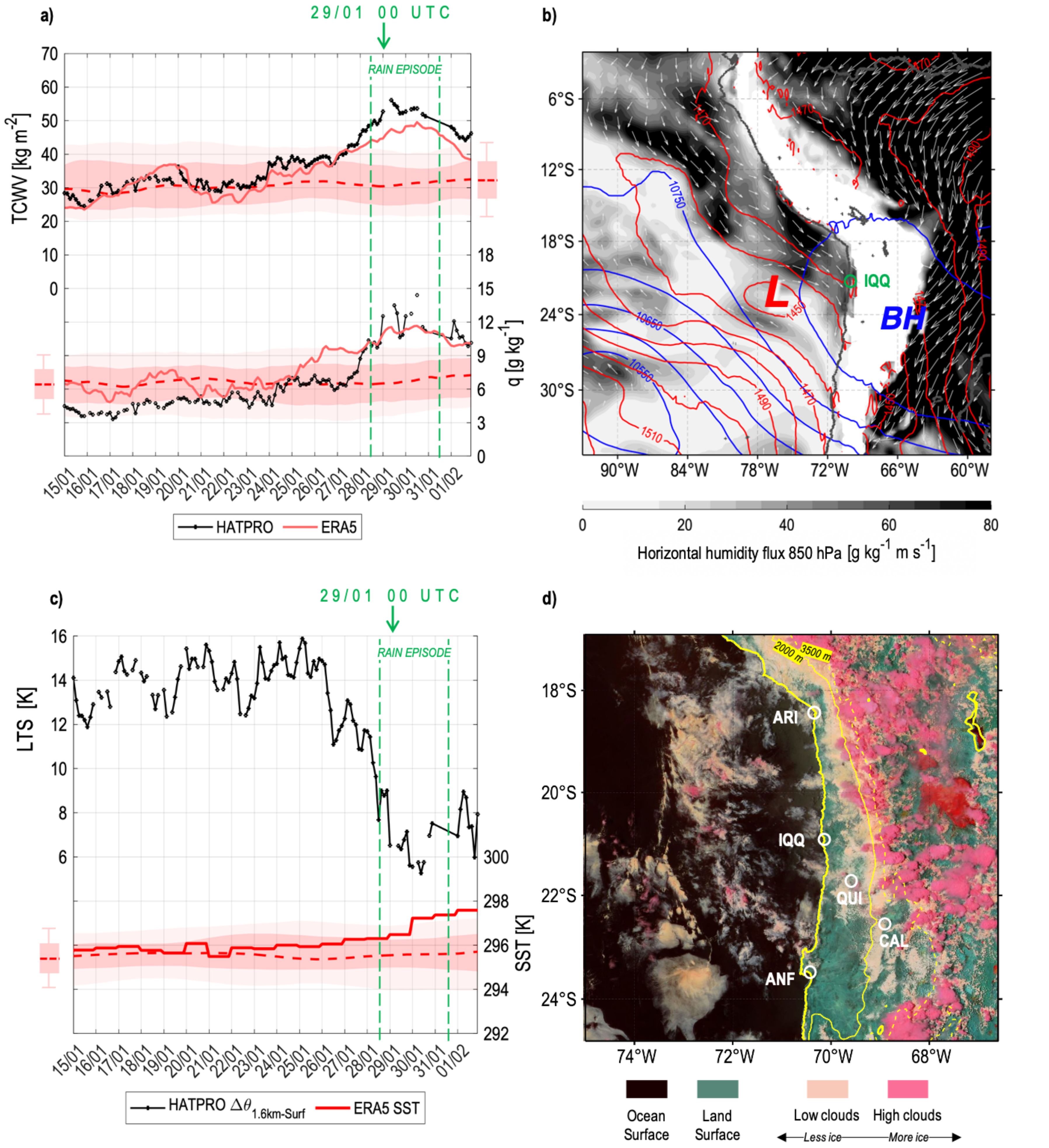
a)
29/01 00 UTC
RAIN EPISODE
TCWV [kg m^-2]
q [g kg^-1]
HATPRO
ERA5
b)
IQQ
L
BH
10750
10650
10550
1470
1490
1450
1510
6°S
12°S
18°S
24°S
30°S
90°W
84°W
78°W
72°W
66°W
60°W
Horizontal humidity flux 850 hPa [g kg^-1 m s^-1]
c)
29/01 00 UTC
RAIN EPISODE
LTS [K]
SST [K]
HATPRO Δθ 1.6km-Surf
ERA5 SST
d)
2000 m
3500 m
ARI
IQQ
QUI
CAL
ANF
18°S
20°S
22°S
24°S
74°W
72°W
70°W
68°W
Ocean Surface
Land Surface
Low clouds
High clouds
Less ice
More ice

Figure 3.

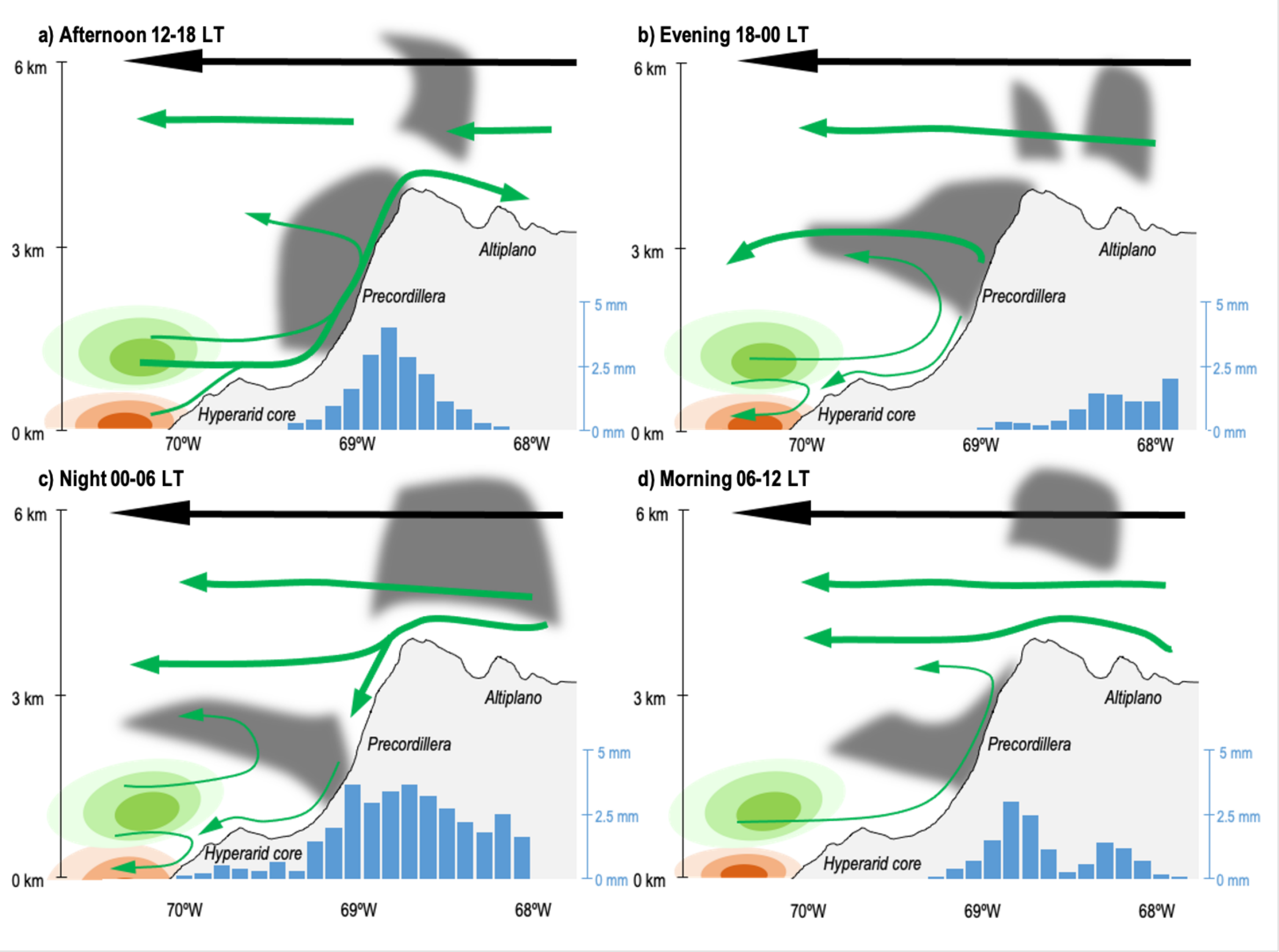
a) Afternoon 12-18 LT
b) Evening 18-00 LT
c) Night 00-06 LT
d) Morning 06-12 LT
6 km
3 km
0 km
Altiplano
Precordillera
Hyperarid core
5 mm
2.5 mm
0 mm
70ºW
69ºW
68ºW

Figure 4.

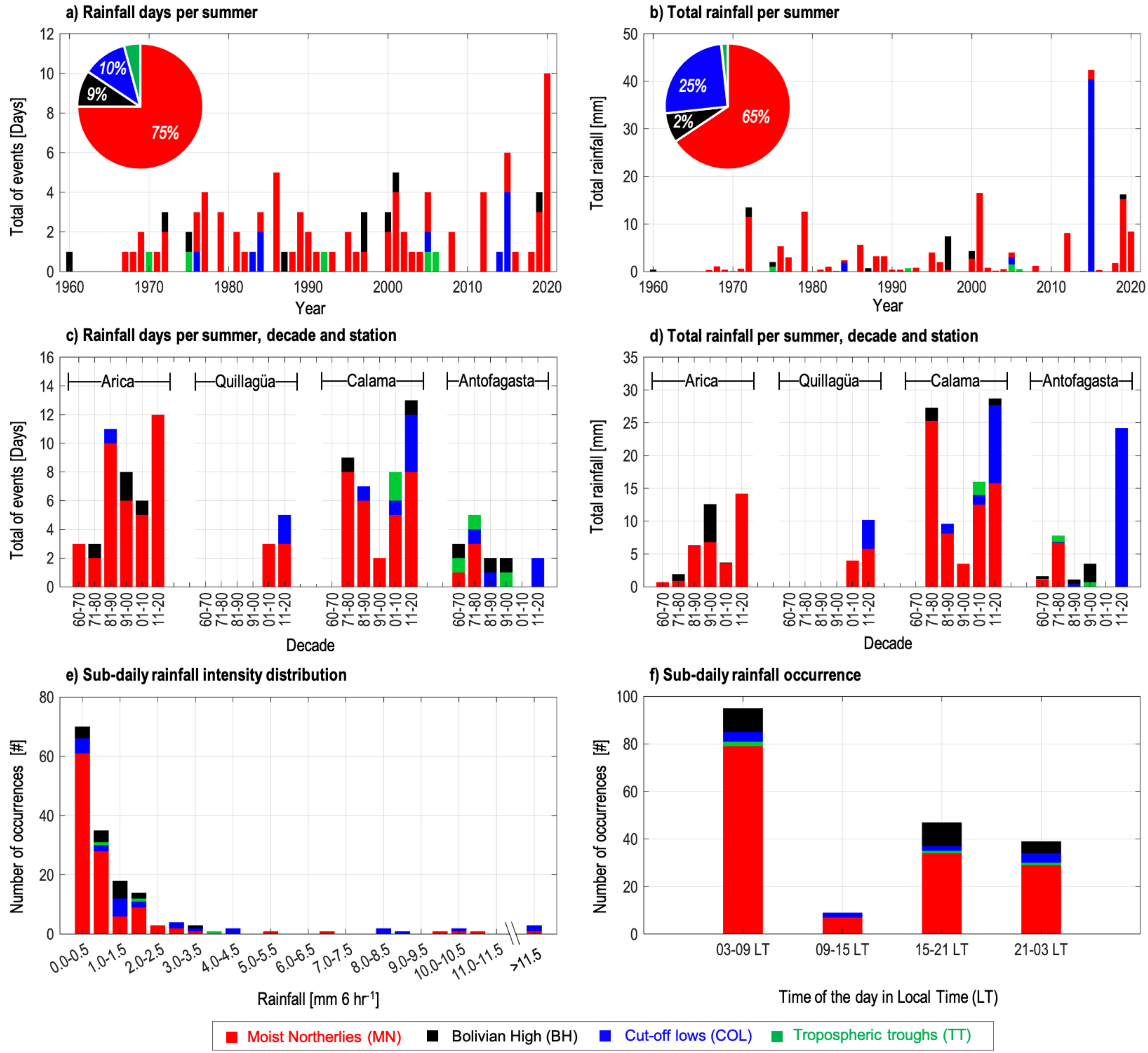

a) Rainfall days per summer
Total of events [Days]
Year
75%
10%
9%
b) Total rainfall per summer
Total rainfall [mm]
Year
65%
25%
2%
c) Rainfall days per summer, decade and station
Total of events [Days]
Decade
Arica
Quillagüa
Calama
Antofagasta
60-70
71-80
81-90
91-00
01-10
11-20
d) Total rainfall per summer, decade and station
Total rainfall [mm]
Decade
e) Sub-daily rainfall intensity distribution
Number of occurrences [#]
Rainfall [mm 6 hr-1]
0.0-0.5
1.0-1.5
2.0-2.5
3.0-3.5
4.0-4.5
5.0-5.5
6.0-6.5
7.0-7.5
8.0-8.5
9.0-9.5
10.0-10.5
11.0-11.5
>11.5
f) Sub-daily rainfall occurrence
Number of occurrences [#]
Time of the day in Local Time (LT)
03-09 LT
09-15 LT
15-21 LT
21-03 LT
Moist Northerlies (MN)
Bolivian High (BH)
Cut-off lows (COL)
Tropospheric troughs (TT)

Figure 5.

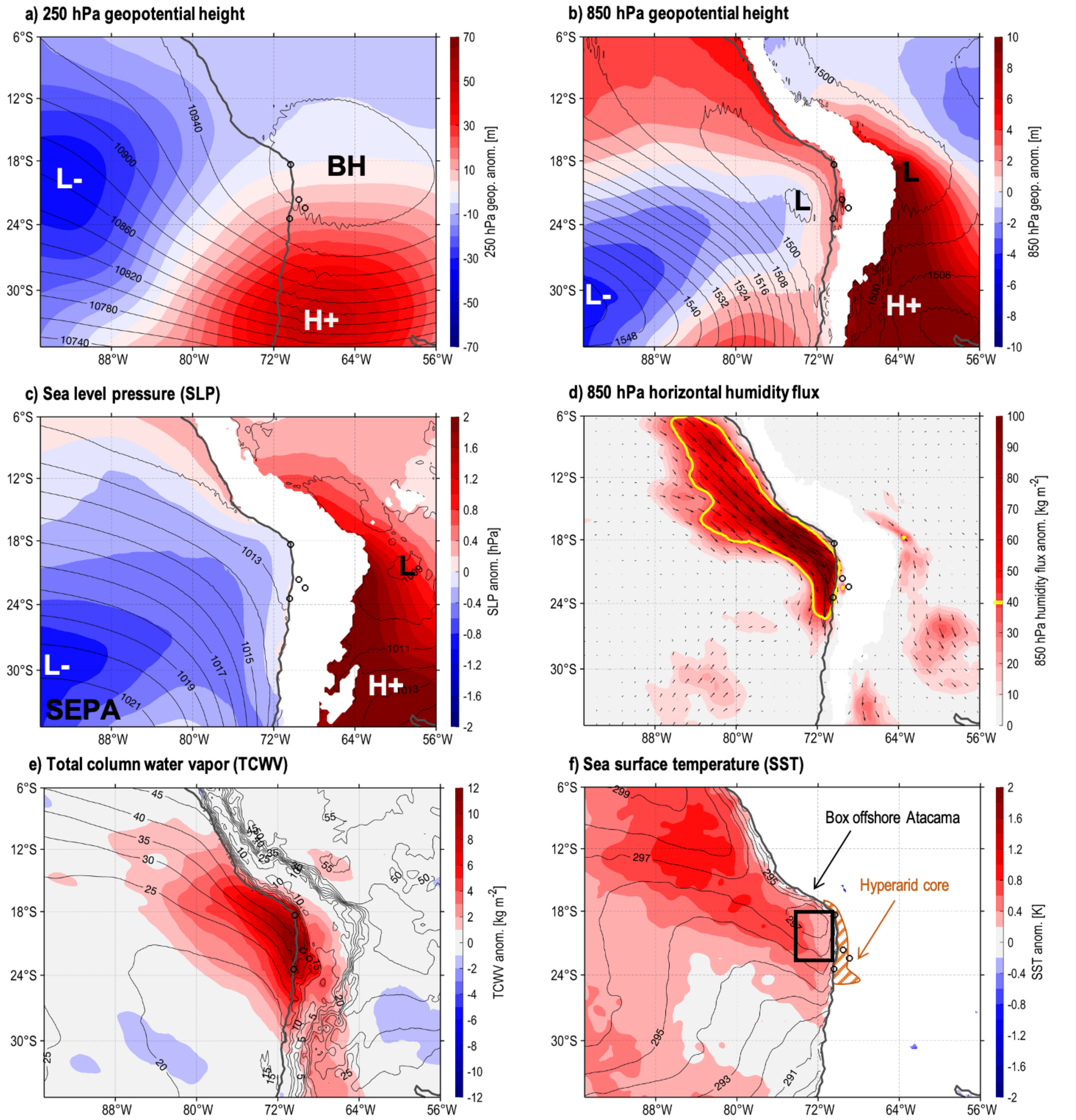
a) 250 hPa geopotential height
BH
L-
H+
250 hPa geop. anom. [m]
b) 850 hPa geopotential height
L
L
L-
H+
850 hPa geop. anom. [m]
c) Sea level pressure (SLP)
L
L-
H+
SEPA
SLP anom. [hPa]
d) 850 hPa horizontal humidity flux
850 hPa humidity flux anom. [kg m-2]
e) Total column water vapor (TCWV)
TCWV anom. [kg m-2]
f) Sea surface temperature (SST)
Box offshore Atacama
Hyperarid core
SST anom. [K]

Figure 6.

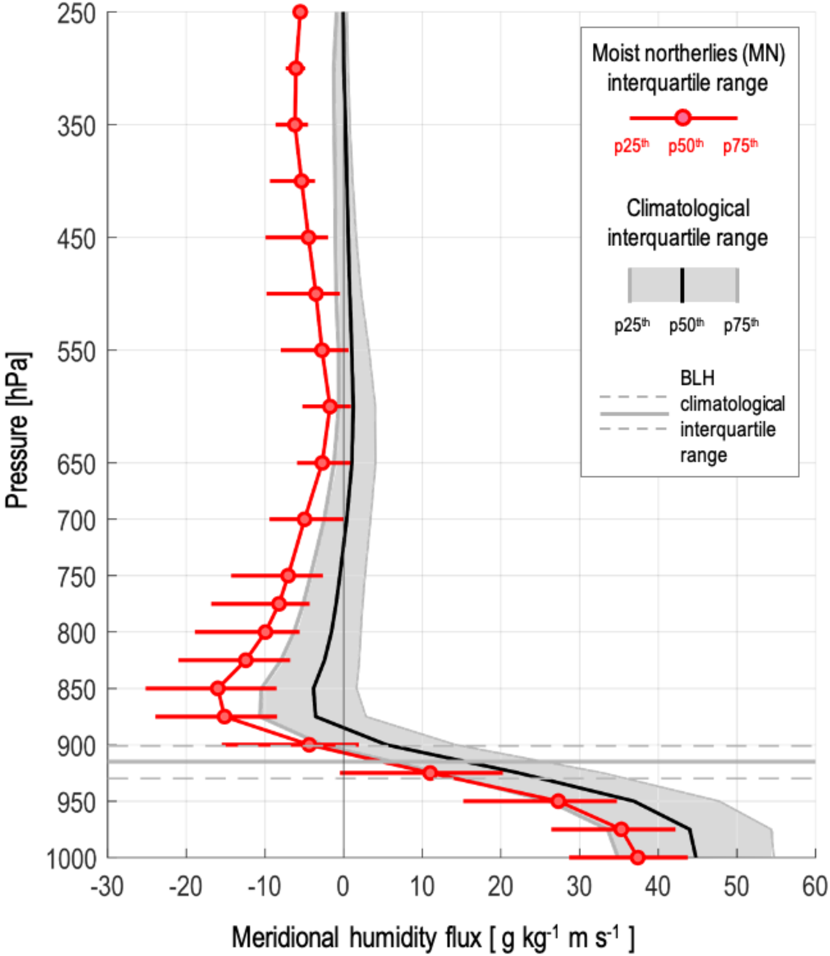

Pressure [hPa]
250
350
450
550
650
700
750
800
850
900
950
1000
-30
-20
-10
0
10
20
30
40
50
60
Meridional humidity flux [g kg-1 m s-1]
Moist northerlies (MN) interquartile range
p25th p50th p75th
Climatological interquartile range
p25th p50th p75th
BLH climatological interquartile range

Figure 7.

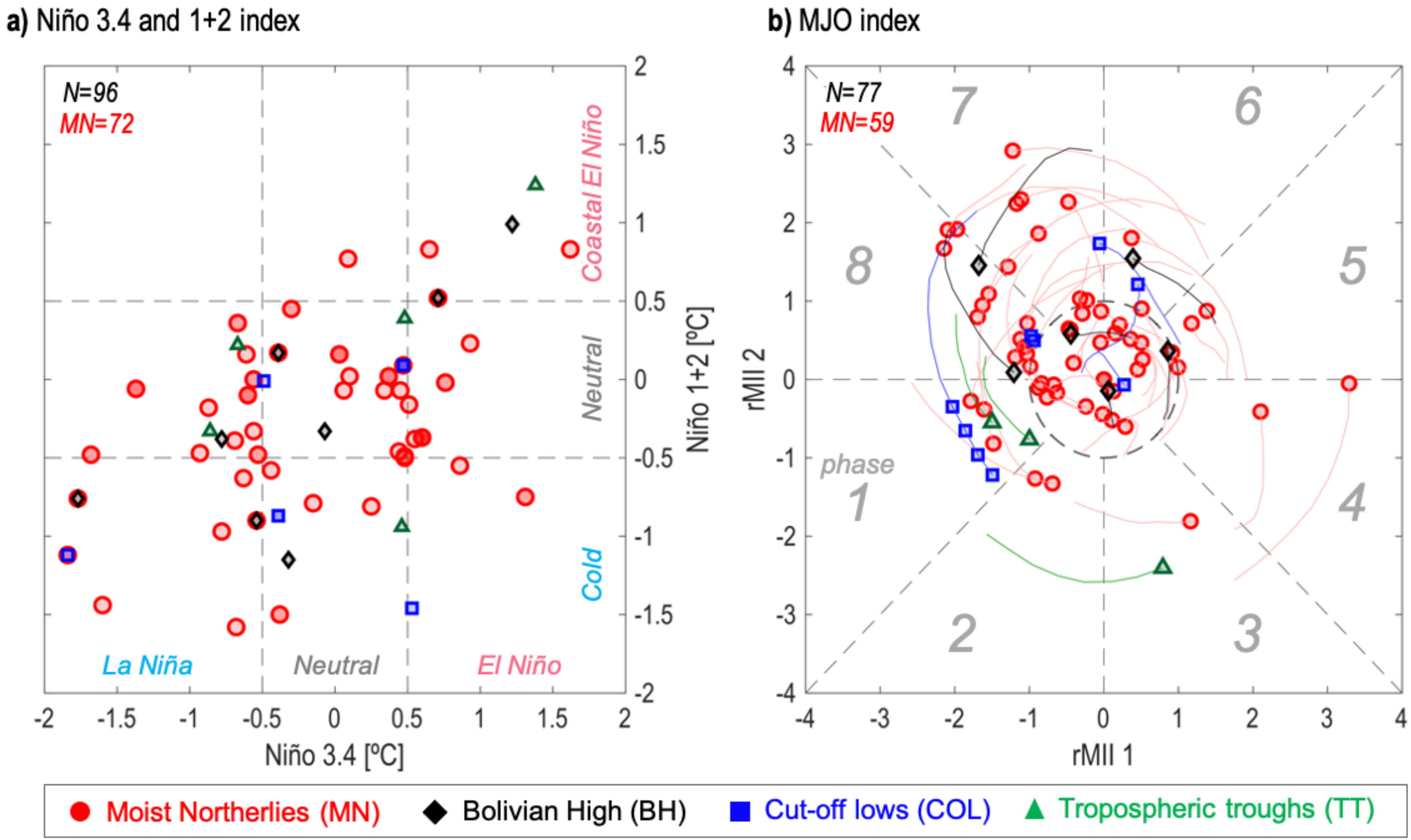
a) Niño 3.4 and 1+2 index
N=96
MN=72
Coastal El Niño
Neutral
Cold
La Niña
Neutral
El Niño
Niño 3.4 [ºC]
Niño 1+2 [ºC]
2
1.5
1
0.5
0
-0.5
-1
-1.5
-2
-2
-1.5
-1
-0.5
0
0.5
1
1.5
2
b) MJO index
N=77
MN=59
7
6
8
5
phase
1
4
2
3
rMII 1
rMII 2
4
3
2
1
0
-1
-2
-3
-4
-4
-3
-2
-1
0
1
2
3
4
Moist Northerlies (MN)
Bolivian High (BH)
Cut-off lows (COL)
Tropospheric troughs (TT)

Figure 8.

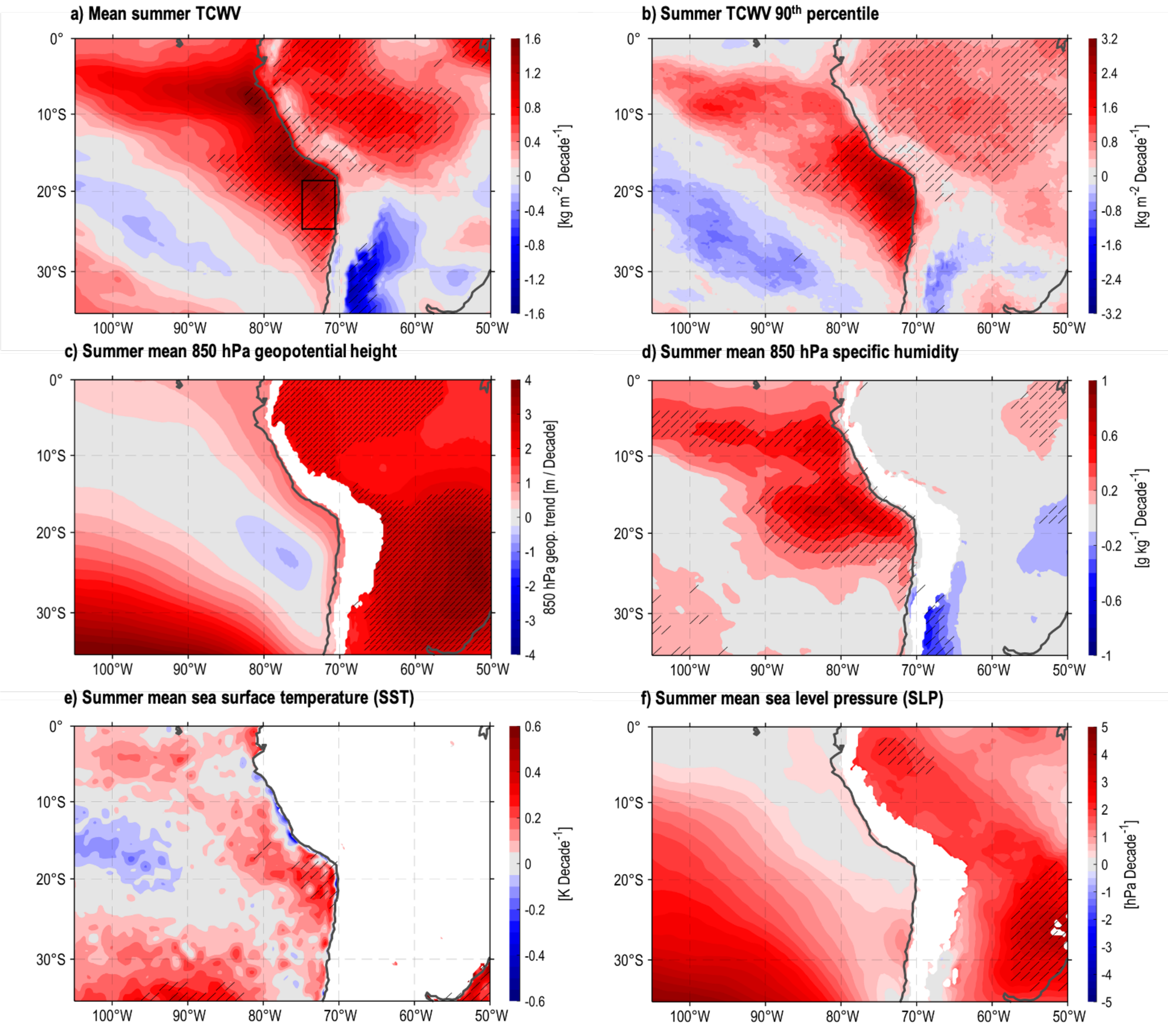
a) Mean summer TCWV
b) Summer TCWV 90th percentile
c) Summer mean 850 hPa geopotential height
d) Summer mean 850 hPa specific humidity
e) Summer mean sea surface temperature (SST)
f) Summer mean sea level pressure (SLP)
0°
10°S
20°S
30°S
100°W
90°W
80°W
70°W
60°W
50°W
[kg m-2 Decade-1]
850 hPa geop. trend [m / Decade]
[g kg-1 Decade-1]
[K Decade-1]
[hPa Decade-1]
1.6
1.2
0.8
0.4
0
-0.4
-0.8
-1.2
-1.6
3.2
2.4
1.6
0.8
-0.8
-1.6
-2.4
-3.2
4
3
2
1
-1
-2
-3
-4
1
0.6
0.2
-0.2
-0.6
-1
0.6
0.4
0.2
-0.2
-0.4
-0.6
5
-5

Figure 9.

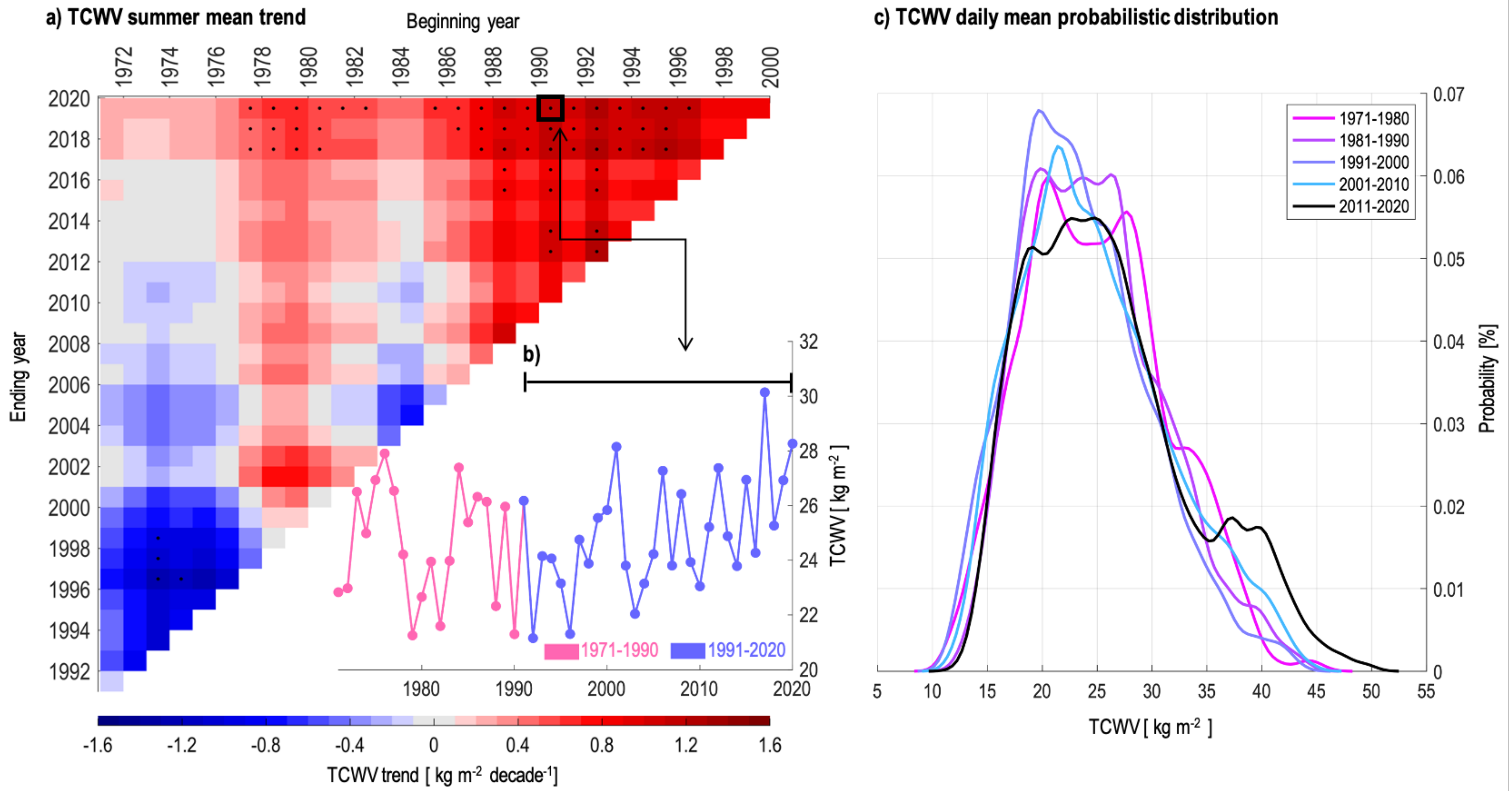
a) TCWV summer mean trend
Beginning year
Ending year
b)
1971-1990
1991-2020
TCWV [kg m-2]
TCWV trend [kg m-2 decade-1]
c) TCWV daily mean probabilistic distribution
1971-1980
1981-1990
1991-2000
2001-2010
2011-2020
Probability [%]
TCWV [kg m-2]

Figure 10.

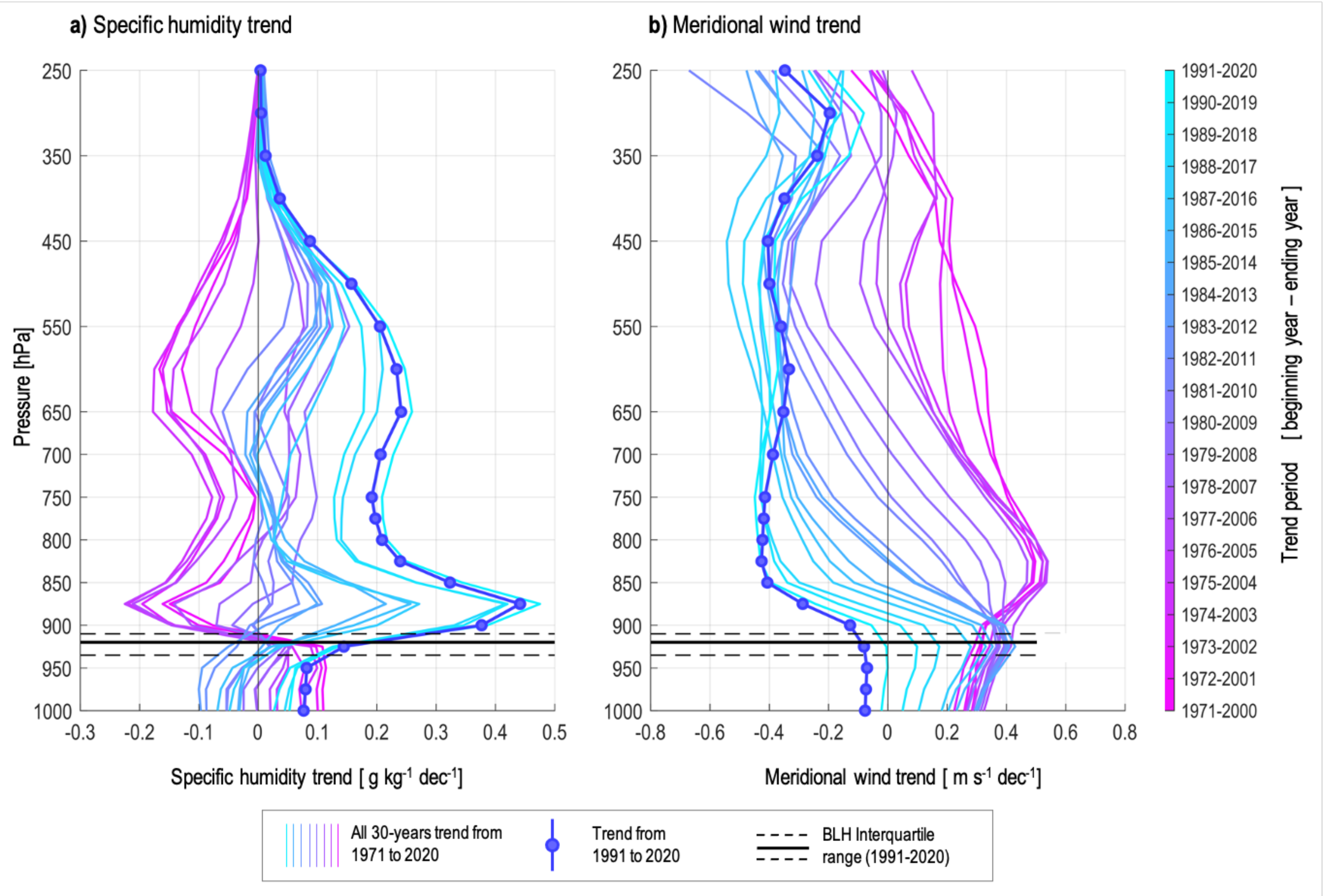
a) Specific humidity trend
b) Meridional wind trend
Pressure [hPa]
250
350
450
550
650
700
750
800
850
900
950
1000
-0.3
-0.2
-0.1
0
0.1
0.2
0.3
0.4
0.5
Specific humidity trend [g kg-1 dec-1]
-0.8
-0.6
-0.4
-0.2
0
0.2
0.4
0.6
0.8
Meridional wind trend [m s-1 dec-1]
Trend period [beginning year – ending year]
1991-2020
1990-2019
1989-2018
1988-2017
1987-2016
1986-2015
1985-2014
1984-2013
1983-2012
1982-2011
1981-2010
1980-2009
1979-2008
1978-2007
1977-2006
1976-2005
1975-2004
1974-2003
1973-2002
1972-2001
1971-2000
All 30-years trend from 1971 to 2020
Trend from 1991 to 2020
BLH Interquartile range (1991-2020)

Supporting Information for "The overlooked role of westerly moisture as a source of summer rainfall in the hyperarid Atacama Desert"

Jose Vicencio Veloso[1], Christoph Böhm[1], Jan H. Schween[1], Ulrich Löhnert[1],

and Susanne Crewell[1]

[1]Institute of Geophysics and Meteorology (IGM), University of Cologne, Cologne, Germany

Contents of this file

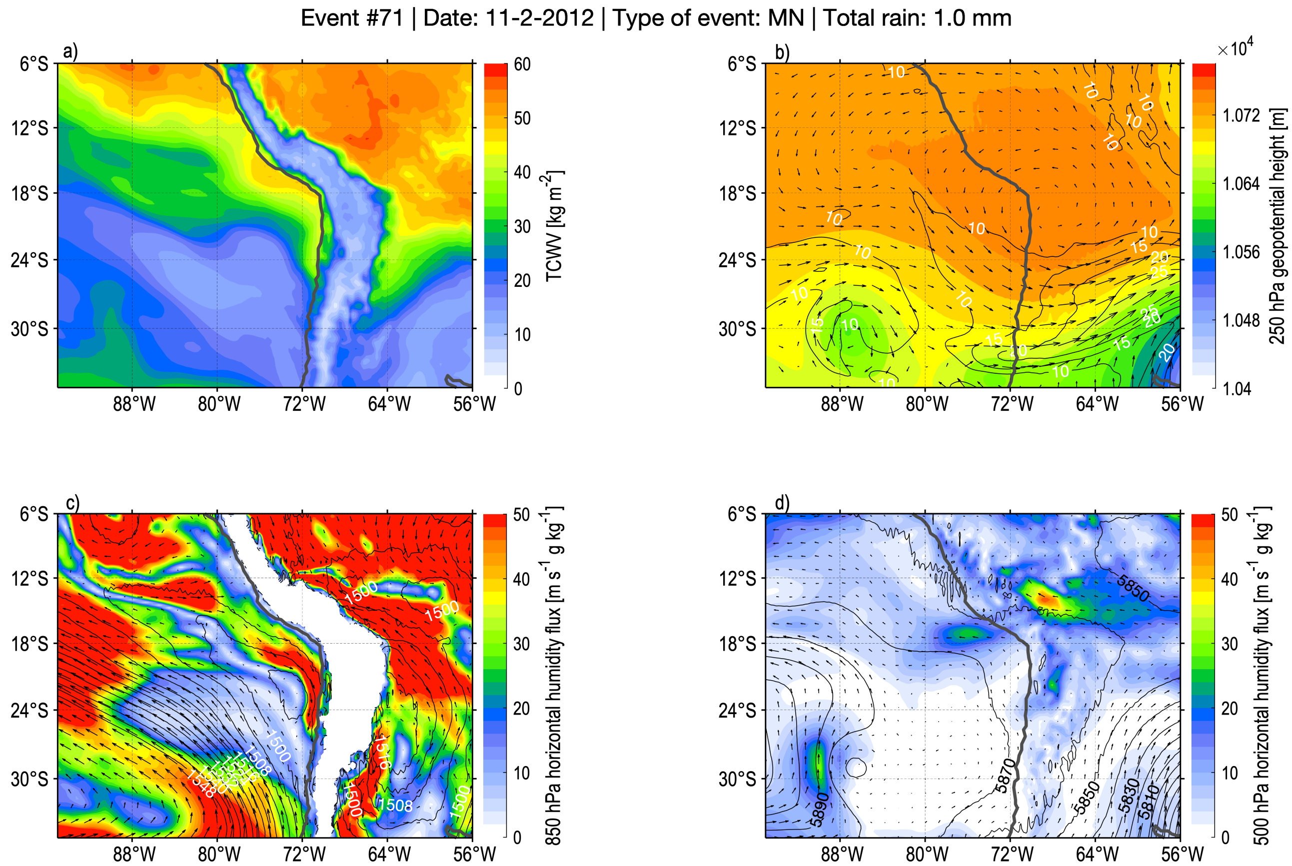

Figure S1. Example a composite for a rainfall day in the Atacama and the synoptic maps used for the classification. The figures for the 96 identified rainfall days are available in Supporting Information 1. At the top of the figure, it is shown the position of the event in chronological order (oldest to recent, according to Table S1), the date (day-month-year), the type of event (MN: Moist Northerlies, BH: Bolivian High, COL: Cut-off Low, and TT: Tropospheric Trough), and the total rainfall as the sum of the four weather stations. (a) TCWV; (b) 250 hPa geopotential height (shaded color) and horizontal wind (arrows), including intensity contours every 10 m s; (c) 850 hPa geopotential height (contour lines) and horizontal humidity flux; and (d) 500 hPa geopotential height (contour lines) and horizontal humidity flux. Data from ERA5.

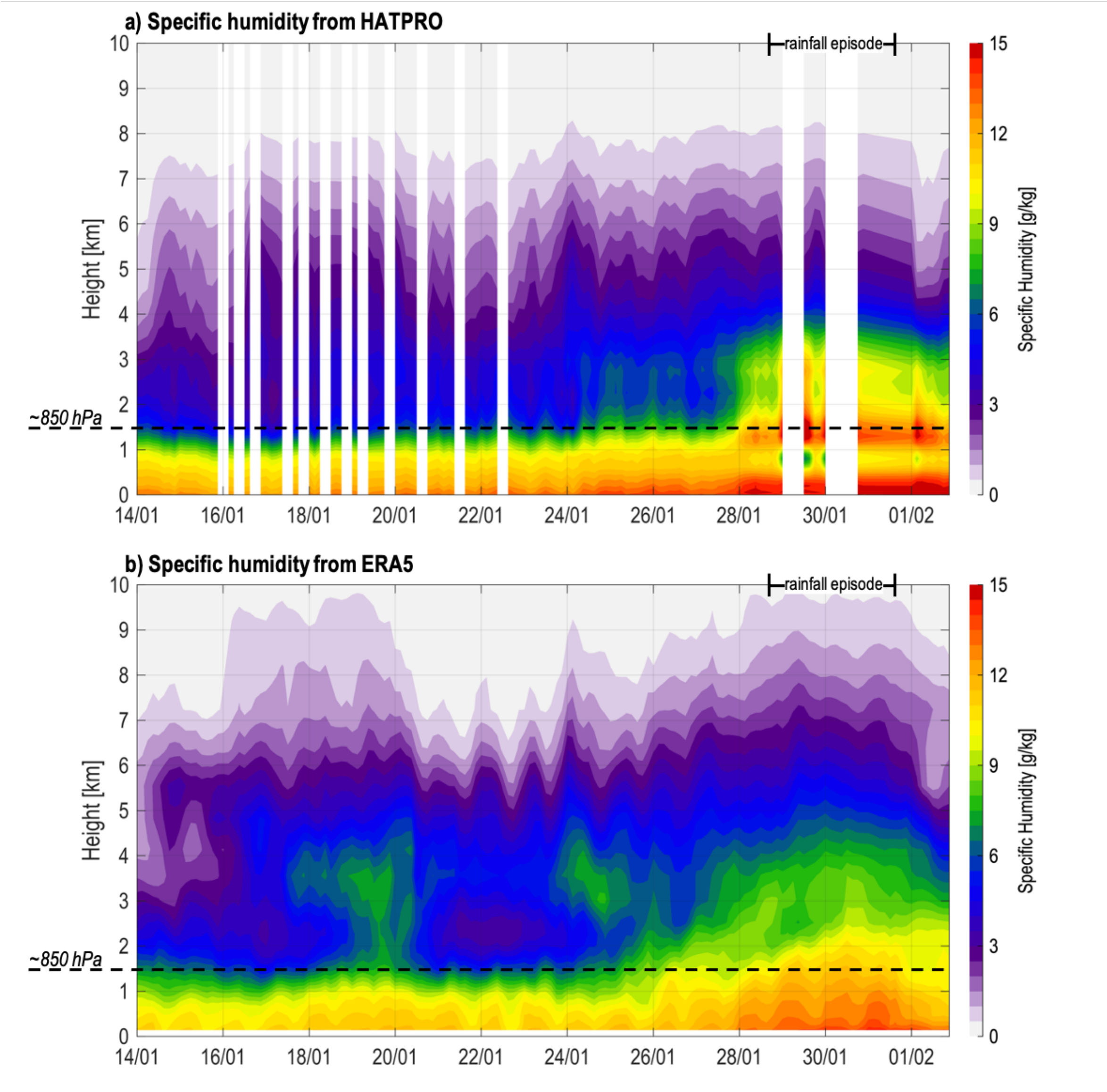

Figure S2. Time-vertical evolution of the specific humidity derived from (a) HATPRO at Iquique Airport (IQQ) and (b) ERA5, averaged from the nearest four grid points around Iquique. The 850 hPa level is shown in a black dashed horizontal line. In (a), vertical white strips show no data in HATPRO.

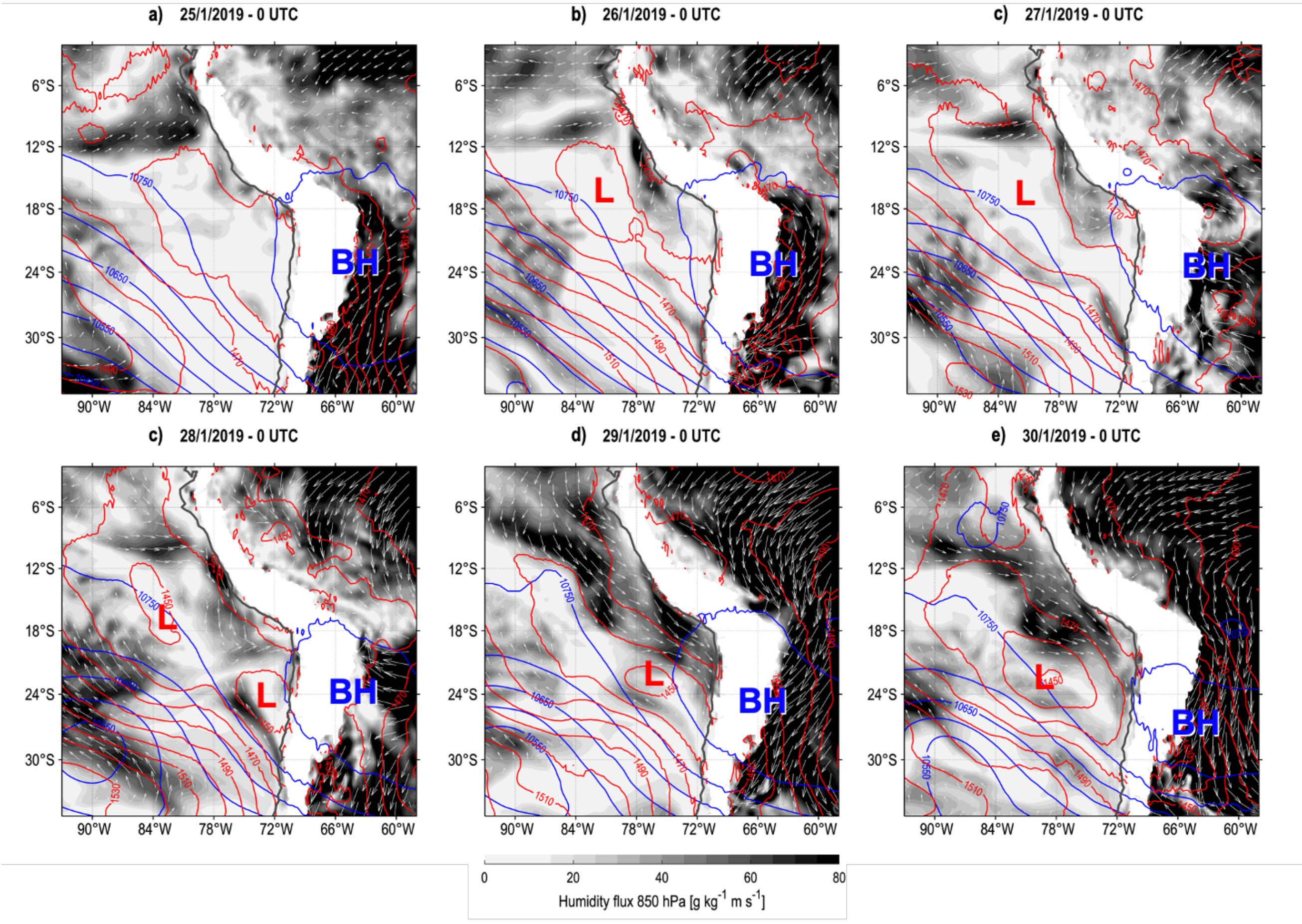

Figure S3. Synoptic evolution from 00 UTC 25 January 2019 to 00 UTC 30 January 2019 of 850 hPa humidity flux (shaded color and arrows above 30 g kg m s), 850 hPa geopotential height (red lines, every 10 m) and 250 hPa geopotential height (black lines, every 50 m). The topography is patched white for altitudes above 850 hPa. 850 hPa low pressure (L) and the 250 hPa Bolivian High (BH) are shown. Data from ERA5.

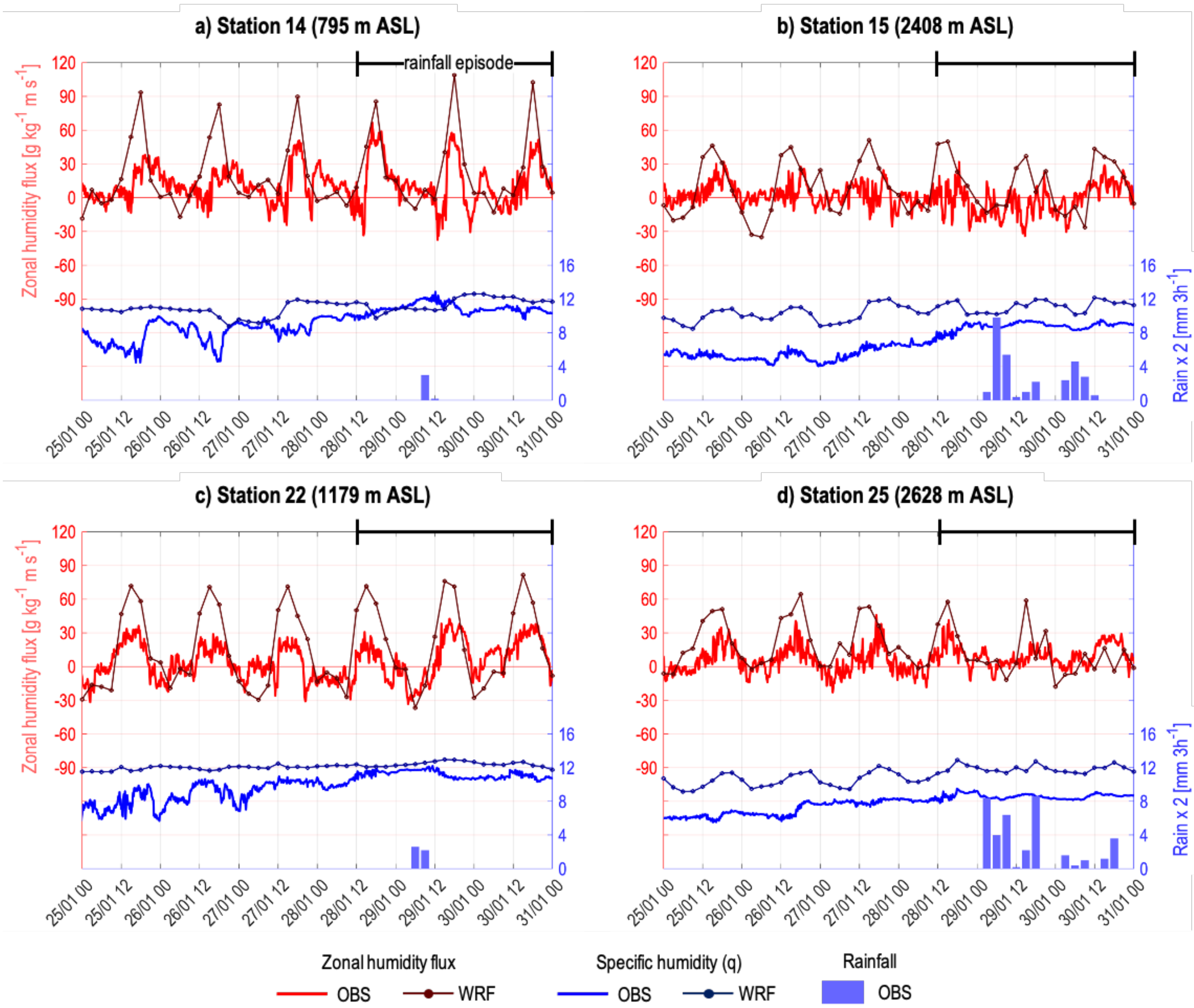

Figure S4. Time series between 25 January 2019 at 00 UTC and 31 January 2019 at 00 UTC of zonal moisture flux (red line) and specific humidity (blue line) from observations (OBS) and WRF nearest grid-point for the CRC1211 weather stations (a) 14, (b) 15, (c) 22 and (d) 25. Precipitation is included only for observations in blue bars. The location of the weather stations is presented in Fig. 1b.

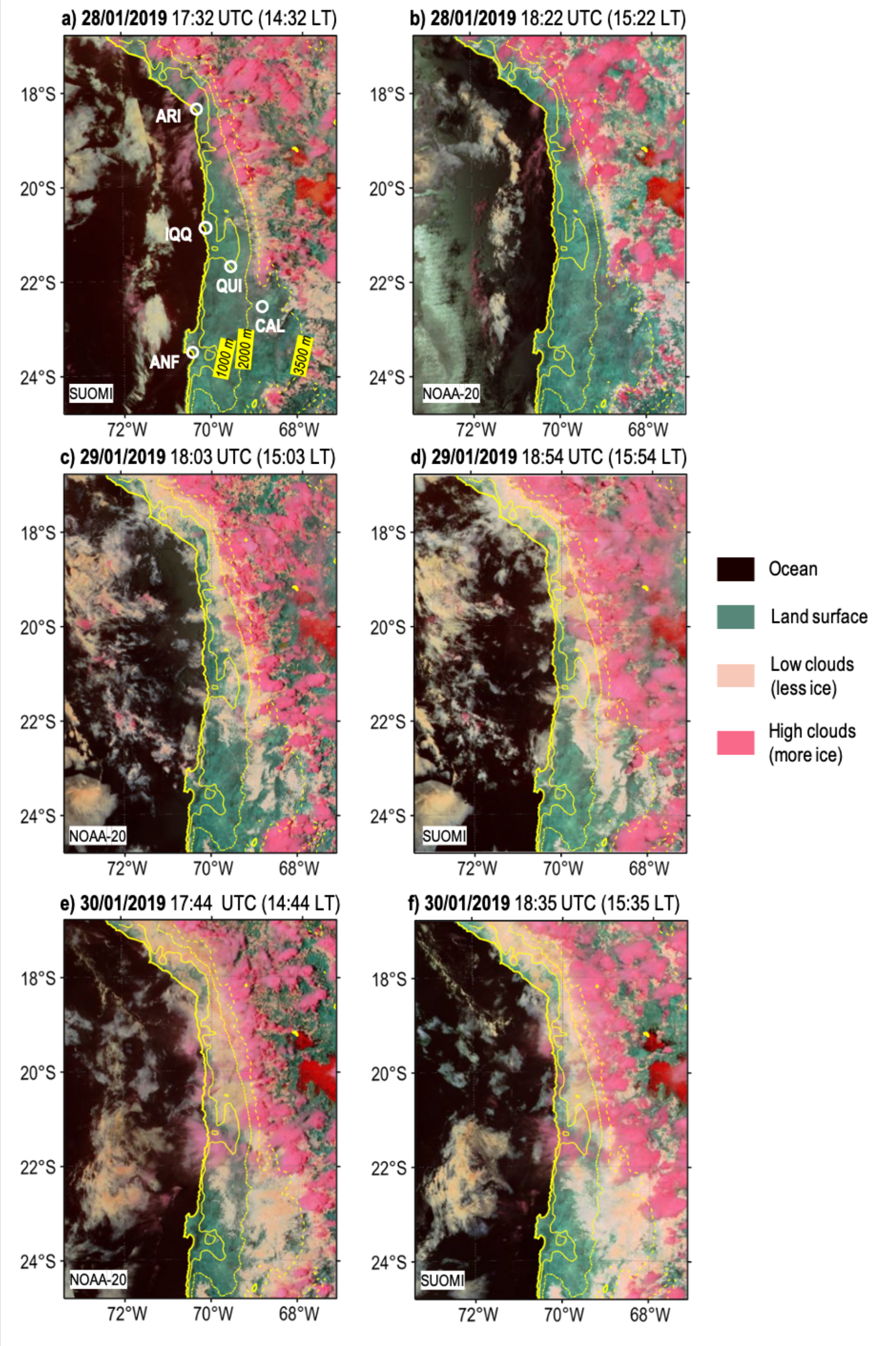

Figure S5. Cloud snow-ice product (Bands M3-I3-M11) from NOAA-20/VIIRS and SUOMI NPP/VIIRS for (a,b) 28 January, (c,d) 29 January and (e,f) 30 January 2019. The same altitude contours are shown in yellow lines at 0 m ASL (thick solid line), 1000 m ASL (thin solid line), 2000 m ASL (thin dotted line) and 3500 m ASL (thin dashed line). In (a), we included the location of the main stations used in this study. Data obtained from https://worldview.earthdata.nasa.gov/

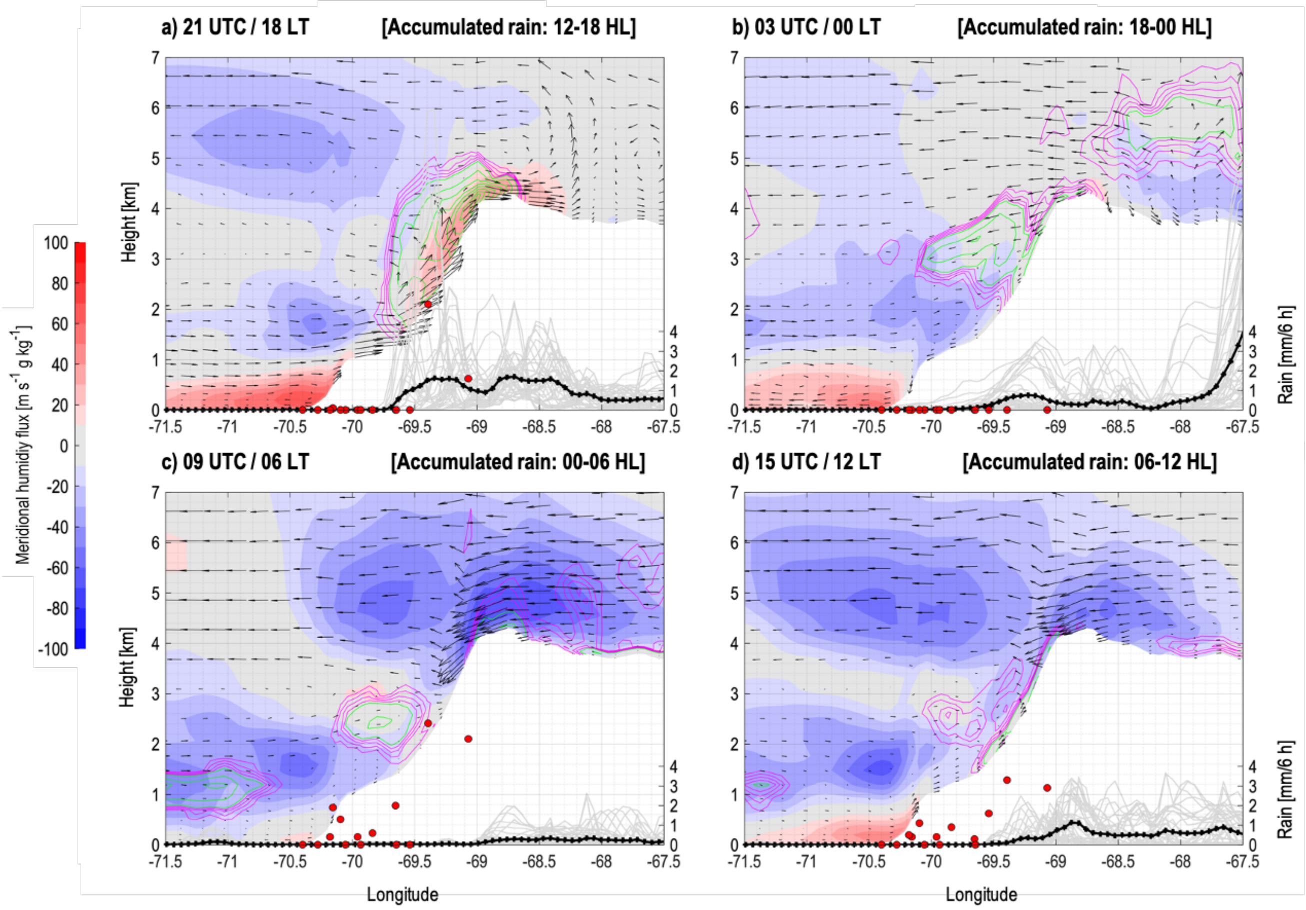

Figure S6. WRF cross-section (average between 19-21°S) evolution from 28 January to 29 January 2019 at 18 LT (a), 00 LT (b), 06 LT (c) and 12 LT (d) of meridional humidity flux (shaded colors), zonal humidity flux (black arrows), cloud liquid water content (magenta for values between 0–0.1 g kg^{-1} every 0.02 g kg^{-1}, and green contours from values between 0.2–0.9 g kg^{-1} every 0.1 g kg^{-1}). The accumulated rainfall (past 6 hours, as indicated in the squared bracket in every panel title) per longitude is plotted in the bottom averaged on x-y latitude (thick black dotted line) and individual latitudes (thin gray lines). Red dots represent observed accumulated rainfall from weather stations in the same period.